A combination of measurements of Higgs boson production and decay using up to 139 fb^{-1} of proton–proton collision data at $\sqrt{s}$ = 13 TeV collected with the ATLAS experiment

The ATLAS Collaboration

A combination of measurements of Higgs boson production cross sections and branching fractions is presented. The combination is based on the analyses of the Higgs boson decay modes $H \rightarrow \gamma\gamma, ZZ^*, WW^*, \tau\tau, b\bar{b}, \mu\mu$, and searches for decays into invisible final states. Up to 139 fb^{-1} of proton–proton collision data collected at $\sqrt{s}$ = 13 TeV with the ATLAS detector are used. Combined cross section measurements are presented for the gluon–gluon fusion and vector-boson fusion processes, and for associated production with vector bosons or top-quarks. The global signal strength, defined as the measured Higgs boson signal yield normalized to its SM prediction, is determined to be $\mu = 1.06 \pm 0.07$. The combined measurement yields an observed (expected) significance for the associated production with a W boson of 6.3 σ (5.2 σ). Measurements in kinematic regions defined within the simplified template cross section framework are also shown. The results are interpreted in terms of modifiers applied to the Standard Model couplings of the Higgs boson to other particles, and are used to set exclusion limits on parameters in two-Higgs-doublet models. No significant deviations from Standard Model predictions are observed.

1 Introduction

Following the discovery of the Higgs boson (H) [1–6] by the ATLAS [7] and CMS [8] experiments, its properties have been probed using proton–proton (pp) collision data produced by the Large Hadron Collider (LHC) at CERN. The coupling properties of the Higgs boson to other Standard Model (SM) particles, such as its production cross sections in pp collisions and decay branching fractions, can be precisely computed within the SM, given the value of the Higgs boson mass. Measurements of these properties can therefore provide stringent tests of the validity of the SM.

Higgs boson production and decay rates were measured using the Run 1 dataset collected in the years 2011 and 2012, through the combination of ATLAS and CMS measurements [9]. These measurements have been extended using the Run 2 dataset recorded by the ATLAS detector from 2015 to 2018, using up to 139 fb^{-1} of pp collision data produced by the LHC. The analyses target several production and decay modes, including: multiple production modes for the $H \to \gamma\gamma$ [10], $H \to ZZ^* \to 4\ell$[1] [11], $H \to WW^*$ [12] and $H \to \tau\tau$ [13] decay channels; the $H \to b\bar{b}$ decay channel produced in three ways: in association with a weak vector boson $V = W$ or Z (VH) [14], in the weak vector-boson fusion (VBF) production process [15], and in association with a top–antitop pair ($t\bar{t}H$) [16–18]; $t\bar{t}H$ in multilepton final states (WW^*, ZZ^* and $\tau\tau$) [16, 18]; the $H \to \mu\mu$ decay channel [19]; and Higgs boson decays into invisible final states ($H \to inv$) produced via the VBF process [20]. This note presents an update of the measurements of Higgs boson properties at $\sqrt{s} = 13$ TeV based on the previous combination using up to 80 fb^{-1} [21]. The following analyses are updated to the full Run 2 dataset: $H \to \gamma\gamma$, $H \to ZZ^* \to 4\ell$, $H \to b\bar{b}$ in VH production, $H \to \mu\mu$, and the search for $H \to inv$ in VBF production, replacing the $H \to inv$ searches based on 36 fb^{-1} [22–25]. A Higgs boson mass value of $m_H = 125.09$ GeV, corresponding to the central value of the combination of ATLAS and CMS measurements in Run 1 [26], is used for SM predictions. The uncertainty in the measured Higgs boson mass is considered in the $H \to \gamma\gamma$, $H \to ZZ^* \to 4\ell$, and $H \to \mu\mu$ analyses where the Higgs boson candidates are reconstructed with high mass resolution, while for the other decay channels it has a negligible impact on the measured signal yields and is therefore neglected. Similar measurements [27–37], as well as their combination [38], have been reported by the CMS Collaboration.

Three of the input analyses, namely $H \to \gamma\gamma$, $H \to ZZ^* \to 4\ell$, and VH, $H \to b\bar{b}$, measure the Higgs boson signal yields in phase-space regions based on the Stage 1.2 simplified template cross-section (STXS) framework [39–42]. These cross sections are defined in the fiducial region $|y_H| < 2.5$, where y_H is the Higgs boson rapidity, and partitioned within each Higgs boson production process into multiple kinematic regions based on the transverse momentum of the Higgs boson, the number of associated jets and their kinematics, and the transverse momentum of associated W or Z bosons. The other analyses use coarser parameterizations as described in Ref. [21].

The note is structured as follows: Section 2 describes the data and simulation samples and Section 3 presents the analyses in individual decay channels which are used as inputs to the combination. Section 4 provides a short description of the statistical procedures. The measurement of the signal strength μ, defined as the ratio of the total Higgs boson signal yield to its SM prediction, is presented in Section 5.1. Measurements of the cross sections of the main production processes within $|y_H| < 2.5$, assuming SM predictions for the branching fractions, are then shown in Section 5.2. The production modes considered are gluon–gluon fusion (ggF), VBF, WH, ZH, $t\bar{t}H$, and associated production with a single top quark (tH). Measurements of cross sections times branching fractions for Higgs boson production and decay processes are shown in Section 5.3. Section 5.4 presents a parameterization where the measured quantities are the

---

[1] Throughout the note ℓ denotes the light leptons e and μ.

ratios of production cross sections and ratios of branching fractions using the ggF cross section and the $H \rightarrow ZZ^*$ branching fraction as denominator, respectively, together with cross section times branching fraction of the process $gg \rightarrow H \rightarrow ZZ^*$. Common systematic uncertainties and modeling assumptions partially cancel out in these ratios, reducing the model dependence of the result. Section 6 presents results in the STXS framework. Potential deviations from SM predictions are then probed in Section 7 with a framework of multiplicative modifiers κ applied to the SM values of Higgs boson couplings [43]. Section 8 presents an interpretation of the data within one benchmark model of beyond-the-SM (BSM) phenomena. Indirect limits on model parameters are set following a methodology similar to that of Ref. [44]. Section 9 summarizes the results.

2 Data and simulated event samples

The results of this note are based on pp collision data collected by the ATLAS experiment[2] [45–47] in the years from 2015 to 2018, with the LHC operating at a center-of-mass energy of 13 TeV. The decay channels, targeted production modes and integrated luminosities of the datasets used in each analysis are shown in Table 1. The uncertainty in the combined 2015–2016 integrated luminosity is 2.1%, and 1.7% in the combined 2015–2018 integrated luminosity [48], obtained using the LUCID-2 detector [49] for the primary luminosity measurements.

Table 1: The decay channels, targeted production modes and integrated luminosity ($\mathcal{L}$) used for each input analysis of the combination. The references for the input analyses and information about which measurements they enter are also provided.

Analysis decay channel	Target Prod. Modes	$\mathcal{L}$ [fb^{-1}]	Ref.	Used in meas.
$H \rightarrow \gamma\gamma$	ggF, VBF, $WH, ZH, t\bar{t}H, tH$	139	[10]	Everywhere
$H \rightarrow ZZ^*$	ggF, VBF, $WH, ZH, t\bar{t}H(4\ell)$	139	[11]	Everywhere
	$t\bar{t}H$ excl. $H \rightarrow ZZ^* \rightarrow 4\ell$	36.1	[16, 18]	Sec. 5 & 7
$H \rightarrow WW^*$	ggF, VBF	36.1	[12]	Sec. 5 & 7
	$t\bar{t}H$		[16, 18]	
$H \rightarrow \tau\tau$	ggF, VBF	36.1	[13]	Sec. 5 & 7
	$t\bar{t}H$		[16, 18]	
$H \rightarrow b\bar{b}$	VBF	24.5 – 30.6	[15]	Sec. 5 & 7
	WH, ZH	139	[14]	Everywhere
	$t\bar{t}H$	36.1	[17, 18]	Sec. 5 & 7
$H \rightarrow \mu\mu$	ggF, VBF, $VH, t\bar{t}H$	139	[19]	Sec. 7.4
$H \rightarrow inv$	VBF	139	[20]	Sec. 7.3 & 7.5

---

[2] ATLAS uses a right-handed coordinate system with its origin at the nominal interaction point (IP) in the center of the detector and the z-axis along the beam pipe. The x-axis points from the IP to the center of the LHC ring, and the y-axis points upwards. Cylindrical coordinates (r, ϕ) are used in the transverse plane, ϕ being the azimuthal angle around the z-axis. The pseudorapidity is defined in terms of the polar angle θ as $\eta = -\ln\tan(\theta/2)$. Angular distance is measured in units of $\Delta R \equiv \sqrt{(\Delta\eta)^2 + (\Delta\phi)^2}$.

Most analyses use a consistent set of simulation programs for the Higgs boson Monte Carlo (MC) samples, as detailed in the following paragraphs. The only exception is the VBF, $H \rightarrow b\bar{b}$ analysis, which uses different samples as described separately at the end of this section. For each Higgs boson decay mode, the branching fraction used corresponds to higher-order state-of-the-art theoretical calculations [39]. The simulated background samples vary channel by channel and are described in the individual references for the input analyses.

Higgs boson production via ggF was simulated using the POWHEG BOX [50–53] NNLOPS implementation [54, 55]. The event generator uses the HNNLO formalism [56] to reweight the inclusive Higgs boson rapidity distribution produced by the next-to-leading order (NLO) generation of $pp \rightarrow H + \text{parton}$, with the scale of each parton emission determined using the MiNLO procedure [57–59]. The PDF4LHC15 [60] parton distribution functions (PDFs) were used for the central prediction and uncertainty. The sample is normalized such that it reproduces the total cross section predicted by a next-to-next-to-next-to-leading-order (N^3LO) QCD calculation with NLO electroweak corrections applied [39, 61–70]. The NNLOPS generator reproduces the Higgs boson p_T distribution predicted by the next-to-next-to-leading-order (NNLO) plus next-to-next-to-leading-logarithm (NNLL) calculation of HRES2.3 [71–73], which includes the effects of top- and bottom-quark masses and uses dynamical normalisation and factorization scales.

The VBF production process was simulated at NLO accuracy in QCD using the POWHEG BOX [74] generator with the PDF4LHC15 set of PDFs. The sample is normalized to an approximate-NNLO QCD cross section with NLO electroweak corrections applied [39, 75–77].

The $qq \rightarrow VH$ production processes were simulated at NLO accuracy in QCD using the POWHEG BOX, GOSAM [78] and MiNLO [57, 79] generators with the PDF4LHC15 set of PDFs. The samples are normalized to cross sections calculated at NNLO in QCD with NLO electroweak corrections [80–89]. The $gg \rightarrow ZH$ process was generated only at leading order (LO), using POWHEG BOX and NLO PDFs and normalized to an NLO computation with next-to-leading-logarithm (NLL) corrections [39, 90].

The $t\bar{t}H$ production process was simulated at NLO accuracy in QCD using the POWHEG BOX [91] generator with the PDF4LHC15 set of PDFs for the $H \rightarrow \gamma\gamma$ and $H \rightarrow ZZ^* \rightarrow 4\ell$ decay processes. For other Higgs boson decays, the MADGRAPH5_AMC@NLO [92, 93] generator was used with the NNPDF3.0 [94] set of PDFs. In both cases the sample is normalized to a calculation with NLO QCD and electroweak corrections [39, 95–98].

In addition to the primary Higgs boson processes, separate samples are used to model lower-rate processes. Higgs boson production in association with a $b\bar{b}$ pair ($b\bar{b}H$) was simulated using MADGRAPH5_AMC@NLO [99] with NNPDF2.3LO PDFs [100] and is normalized to a cross section calculated to NNLO in QCD [39, 101–103]. The sample includes the effect of interference with the ggF production mechanism. Higgs boson productions in association with a single top quark both in t-channel (tHq) and with an additional W boson (tHW) were produced at NLO accuracy using MADGRAPH5_AMC@NLO with the NNPDF3.0 PDF set [104] in the $H \rightarrow \gamma\gamma$ and $H \rightarrow ZZ^* \rightarrow 4\ell$ decay processes. For $t\bar{t}H$, $H \rightarrow b\bar{b}$ and multilepton analyses, tHq and tHW samples were also generated with MADGRAPH5_AMC@NLO, but the accuracy of the tHq sample was LO in QCD. There were also other differences as detailed in Ref. [16, 17]. The tH samples are normalized to NLO QCD calculations [39, 105, 106] in all cases.

The parton-level events were input to PYTHIA8 [107] or HERWIG++ [108] to model the Higgs boson decay, parton showering, hadronization, and multiple parton interaction (MPI) effects. The generators were interfaced to PYTHIA8 for all samples except for tHW in $t\bar{t}H$, $H \rightarrow b\bar{b}$ and multilepton analyses, which used HERWIG++ instead. For PYTHIA8 the AZNLO [109] and A14 [110] parameter sets were used, and for HERWIG++ its UEEE5 parameter set was used.

Higgs boson decay branching fractions were computed using HDECAY [111–113] and PROPHECY4F [114–116].

In the all-hadronic channel of the VBF, $H \rightarrow b\bar{b}$ analysis, the POWHEG BOX generator with the CT10 [117] set of PDFs was used to simulate the ggF [118] and VBF production processes, and interfaced with PYTHIA8 for parton shower. In the photon channel of the VBF, $H \rightarrow b\bar{b}$ analysis, VBF and ggF production in association with a photon was simulated using the MADGRAPH5_AMC@NLO generator with the PDF4LHC15 set of PDFs, and also using PYTHIA8 for parton shower. For both channels, contributions from VH and $t\bar{t}H$ production were generated using the PYTHIA8 generator with the NNPDF3.0 set of PDFs, and using the MADGRAPH5_AMC@NLO generator interfaced with HERWIG++ and the NLO CT10 set of PDFs, respectively.

The particle-level Higgs boson events were passed through a GEANT 4 [119] simulation of the ATLAS detector [120] and reconstructed using the same analysis software as used for the data. Event pileup is included in the simulation by overlaying inelastic pp collisions, such that the average number of interactions per bunch crossing reproduces that observed in the data. The inelastic pp collisions were simulated with PYTHIA8 using the MSTW2008LO [121] set of PDFs with the A2 [122] set of tuned parameters or using the NNPDF2.3LO set of PDFs with the A3 [123] set of tuned parameters.

3 Individual channel measurements

Brief descriptions of the updated analyses for the present combination are given below. More details can be found in the individual analysis references listed in each section. Descriptions for the other analyses can be found in the previous combination [21] and their corresponding references given in Section 1 and also Table 1. The overlap between the event selections of the analyses included in the combination is found to be negligible.

Among all the input analyses, $H \rightarrow \mu\mu$ and VBF, $H \rightarrow inv$ are only considered in a subset of the results that are presented in Section 7. The remaining ones are included in every set of results except for the STXS measurements (Section 6), which only include $H \rightarrow \gamma\gamma$, $H \rightarrow ZZ^* \rightarrow 4\ell$, and VH, $H \rightarrow b\bar{b}$ channels.

3.1 $H \rightarrow \gamma\gamma$

The $H \rightarrow \gamma\gamma$ analysis [10] requires the presence of two isolated photons within the pseudorapidity range $|\eta| < 2.37$, excluding the region $1.37 < |\eta| < 1.52$ corresponding to the transition between the barrel and endcap sections of the electromagnetic calorimeter. The transverse momenta of the leading and subleading photons are required to be greater than $0.35m_{\gamma\gamma}$ and $0.25m_{\gamma\gamma}$ respectively, where $m_{\gamma\gamma}$ is the invariant mass of the diphoton system. The event reconstruction and selection procedures are detailed in Ref. [10].

The reconstructed event categorisation is significantly updated as compared to the previous iteration [21]. In the previous analysis, the categorisation proceeded sequentially for each production mode, in order of increasing cross-section. The present categorisation follows a two-step approach with an initial global categorisation of events into 44 categories, chosen to closely match those of the Stage 1.2 STXS regions described in Section 6.1. This is followed by a subdivision of each category into up to three additional categories based on the separation of the signal from the continuum background.

For the first step, the global categorisation uses a multiclass BDT, which is trained on an inclusive Higgs boson signal sample with the signal yield in each STXS bin reweighted to the same value for improved performance. For each reconstructed event, the multiclass BDT produces a score for each STXS bin. These scores are multiplied with an additional set of weights derived from an iterative procedure aiming to minimize the measurement uncertainty. The event is eventually assigned to the category which corresponds to the STXS bin with the highest final score. This procedure leads to a reduction of both the measurement uncertainties and the linear correlations between the measurements in the different regions.

The second step in the categorisation uses binary BDTs to improve the separation of the signal from the continuum background. A separate BDT is trained for each production process in the STXS framework. Each category from the first step is split into two or three sub-categories based on the binary BDT distribution if the improvement is more than 5% in the expected significance. This second step results in 88 reconstructed event categories in total. Finally, the distribution of $m_{\gamma\gamma}$ is used to separate the Higgs boson signal from continuum background processes in each category.

3.2 $H \rightarrow ZZ^* \rightarrow 4\ell$

The $H \rightarrow ZZ^* \rightarrow 4\ell$ analysis [11] requires the presence of at least two same-flavor and opposite-charge light-lepton pairs, with a four-lepton invariant mass $m_{4\ell}$ in the range $115\,\text{GeV} < m_{4\ell} < 130\,\text{GeV}$. The analysis follows the strategy described in the previous combination publication [21], but employs improved lepton isolation to mitigate the impact of pileup and the jet reconstruction now follows a particle flow approach. Both the number of STXS bins and event categories have slightly increased, improving the sensitivity of the measurement. The $m_{4\ell}$ side-bands 105 – 115 GeV and 130 – 160 GeV are introduced as categories to constrain the dominant non-resonant ZZ^* background for most reconstruction signal categories, while the 105 – 115 GeV and 130 – 350 GeV side-bands are used to constrain the $t\bar{t}H$ background.

To distinguish the $t\bar{t}H$, VH, VBF, and ggF production modes and to enhance the purity of each kinematic selection, 12 mutually exclusive reconstructed event categories based on the presence of jets and additional leptons in the final state are defined. Two $t\bar{t}H$ categories are defined for leptonic and fully hadronic decays requiring an additional lepton and multiple jets, some with a b-tag, for the former, and four or five jets and one or more b-tags for the latter. Events with two jets are separated into a BSM-like category, with leading jet invariant mass m_{jj} larger than 120 GeV and four lepton transverse momentum $p_T^{4\ell}$ larger than 200 GeV, and the remainder are in a category for the bulk of the VBF and $V(\rightarrow qq)H$ events. The 0- and 1-jet events are expected to be mostly from the ggF process and classified into five categories mostly following the STXS classification described in Section 6.1, according to the four lepton transverse momentum $p_T^{4\ell}$. There is a 0-jet category with $p_T^{4\ell}$ above 100 GeV which improves the discrimination between VH ($V \rightarrow \ell\nu, \nu\nu$) and ggF, and a 1-jet category with $p_T^{4\ell}$ above 200 GeV which is considered a BSM-like category. To further increase the sensitivity of the cross-section measurements in the STXS bins, multivariate discriminants using neural networks (NNs) are introduced in most of the reconstructed signal event categories as observables used in the statistical fit.

3.3 $VH, H \rightarrow b\bar{b}$

The measurement of $H \rightarrow b\bar{b}$ in the VH production mode [14] considers final states containing at least two jets, of which exactly two must be tagged as containing b-hadrons. Either zero (with large E_T^{miss}),

one or two charged leptons are also required, exploring the associated production of a Higgs boson with a W or Z boson decaying leptonically as $Z \to \nu\nu$, $W \to \ell\nu$, or $Z \to \ell\ell$. Contributions from $W \to \tau\nu$ and $Z \to \tau\tau$ decays in which the τ-leptons subsequently decay into electrons or muons are also included. Since the previous publications [124, 125] a number of improvements are included: enhanced object calibrations, more coherent categorisation between the event selection and the STXS binning, re-optimised multivariate discriminants including the addition of more information, redefined signal and control regions, a significant increase in the effective number of simulated events and re-derived background modelling uncertainties, including using a multivariate approach to estimate the modelling uncertainty in the dominant backgrounds.

To enhance the signal sensitivity, the selected candidate events are classified according to the charged-lepton multiplicity, the vector-boson transverse momentum p_T^V, and the jet multiplicity. For final states with zero or one lepton, two p_T^V regions are defined: $150 - 250$ GeV and ≥ 250 GeV. In two-lepton final states, in addition to these two regions, 75 GeV $\leq p_T^V < 150$ GeV is defined. The p_T^V thresholds are chosen to select regions with strong experimental sensitivity, and match the STXS definitions described in Section 6.1. The zero and one lepton regions are finally separated into categories with either exactly two or three reconstructed jets, and the two lepton regions are separated into categories with either two or at least three jets. Topological and kinematic selection criteria are applied within each of the resulting categories. BDTs incorporating the event kinematics and topology, and b-tagging information, in addition to the dijet invariant mass, are employed in each lepton channel and analysis region to separate the signal process from the sum of the expected background processes.

3.4 $H \to \mu\mu$

The $H \to \mu\mu$ search [19] employs a similar technique to the $H \to \gamma\gamma$ analysis [10]: a resonance at 125 GeV is searched for in the invariant mass spectrum $m_{\mu\mu}$ for pairs of opposite-charge muons on top of a continuum background, dominated by the Drell-Yan contribution for the inclusive spectrum.

Events are classified into twenty mutually exclusive categories defined to exploit the topological and kinematic differences between the background processes and the different Higgs boson production modes, ggF, VBF, VH and $t\bar{t}H$. A $t\bar{t}H$ region is defined by requiring events with an extra lepton and a b-tagged jet, and two VH regions are defined by requiring events with either one or two extra leptons, and no b-tagged jet. BDTs are trained in each of these regions and used to apply selections to define one $t\bar{t}H$ category, two VH one-lepton categories, and one VH di-lepton category. The remaining events are classified according to the number of jets: zero, one and two or more. Four categories are defined for VBF using a BDT applied to the 2-jet events, and three additional BDTs, one per jet multiplicity, are used to define a further 12 categories for the 0-, 1- and remaining 2-jet events. The updated analysis has improved sensitivity compared with the one used in the previous combination [21]. This analysis is only included in the results presented in Section 7.4.

3.5 VBF, $H \to inv$

The search for decays of the Higgs boson into invisible final states in the VBF topology [20] is carried out by selecting events with missing transverse momentum E_T^{miss} larger than 200 GeV, and a soft track term of E_T^{miss} less than 20 GeV. In addition, at least two jets are required with the leading two in opposite longitudinal hemispheres having a pseudorapidity difference $|\Delta\eta_{jj}| > 3.8$, an azimuthal angle difference

$\Delta\phi_{jj} < 2.0$, and an invariant mass $m_{jj} > 0.8$ TeV. The vector sum of the transverse momenta of all the selected jets is required to be larger than 180 GeV. Events with isolated lepton or photon candidates, as well as those containing more than one jet tagged as originating from a b-hadron, are rejected.

Eleven signal categories are defined. Ten categories are defined in m_{jj} and $\Delta\phi_{jj}$ bins with events containing exactly two jets, and an additional category contains events with three or four jets. Control regions are introduced to constrain the main background process $V+$jets and the small contribution from multi-jet processes. Other background processes are estimated using MC simulations.

In this note, this analysis is included only in the coupling tests presented in Sections 7.3 and 7.5.

4 Statistical model

The statistical methods used in this paper follow those of Ref. [9]. The results of the combination are obtained from a likelihood function defined as the product of the likelihoods of each input analysis. These are themselves products of likelihoods computed in mutually exclusive regions selected in the analysis, referred to as analysis categories.

The number of signal events in each analysis category k is expressed as

$$n_k^{\text{signal}} = \mathcal{L}_k \sum_i \sum_f (\sigma \times B)_{if} (A \times \epsilon)_{if,k} \tag{1}$$

where the sum runs over production modes i ($i =$ ggF, VBF, WH, ZH, $t\bar{t}H$, ...) or the partitioned STXS bins as described in Section 6.1, and decay final states f ($f = \gamma\gamma, ZZ^*, WW^*, \tau\tau, b\bar{b}, \mu\mu, \ldots$), $\mathcal{L}_k$ is the integrated luminosity of the dataset used in category k, and $(A \times \epsilon)_{if,k}$ is the acceptance times efficiency factor in category k for production mode i and final state f. The cross section times branching fraction $(\sigma \times B)_{if}$ for each relevant pair (i, f) are the parameters of interest of the model. The measurements presented in this paper are obtained from fits in which these products are free parameters (Section 5.3), or in which they are re-expressed in terms of smaller sets of parameters: of a single signal-strength parameter μ (Section 5.1), of the cross sections σ_i in each of the main production modes (Section 5.2), of ratios of cross sections and branching fractions (Sections 5.4 and Section 6.2), of coupling modifiers (Section 7), or of parameters of the BSM model (Section 8). Additional parameters, referred to as nuisance parameters, are used to describe systematic uncertainties and background quantities that are constrained by sidebands or control regions in data. The estimates of those nuisance parameters related to systematic uncertainties are modeled with distributions that correspond to auxiliary measurements (e.g. Gaussian), and relevant terms are included in the likelihood function.

Systematic uncertainties that affect multiple analyses are modeled with common nuisance parameters to propagate the effects of these uncertainties coherently to all measurements. The assessment of the associated uncertainties varies between data samples, reconstruction algorithms and software releases, leading to differences particularly between analyses performed using the full Run 2 dataset and those using 2015 and 2016 data only. Between these two sets of analyses, components of systematic uncertainties in the luminosity, the electron/photon resolution and energy scale, and in the electron reconstruction and identification efficiencies are also treated as correlated. Uncertainties due to the limited number of simulated events used to estimate expected signal and background yields are included using the simplified version of the Beeston–Barlow technique [126] implemented in the HISTFACTORY tool [127]. They are counted among the systematic uncertainties.

Theory uncertainties in the signal, such as missing higher-order QCD corrections and PDF-induced uncertainties, affect the expected signal yields of each production and decay process, as well as the signal acceptance in each category. These uncertainties are modeled by a common set of nuisance parameters in most channels. For the signal-strength (Section 5.1) and coupling modifier (Section 7) results and constraints on new phenomena (Section 8), which rely on the comparison of measured and SM-expected yields, both the acceptance and signal yield uncertainties are included. For the cross-section and branching fraction results from Sections 5.2 through 6, only acceptance uncertainties are considered. The effects of correlations between Higgs boson branching fractions are modeled using the correlation model specified in Ref. [39]. Uncertainties due to dependencies on SM parameter values and missing higher-order effects are applied to the partial decay widths and propagated to the branching fractions. The uncertainties due to modeling of background processes are typically treated as uncorrelated between analyses.

The measurement of the parameters of interest is carried out using a statistical test based on the profile likelihood ratio [128],

$$\Lambda(\boldsymbol{\alpha}) = \frac{L(\boldsymbol{\alpha}, \hat{\hat{\boldsymbol{\theta}}}(\boldsymbol{\alpha}))}{L(\hat{\boldsymbol{\alpha}}, \hat{\boldsymbol{\theta}})} \ ,$$

where $\boldsymbol{\alpha}$ and $\boldsymbol{\theta}$ are respectively the parameters of interest and the nuisance parameters. In the numerator, the nuisance parameters are set to their profiled values $\hat{\hat{\boldsymbol{\theta}}}(\boldsymbol{\alpha})$, which maximize the likelihood function for fixed values of the parameters of interest $\boldsymbol{\alpha}$. In the denominator, both the parameters of interest and the nuisance parameters are set to the values $\hat{\boldsymbol{\alpha}}$ and $\hat{\boldsymbol{\theta}}$ respectively which jointly maximize the likelihood.

In the asymptotic regime, in which the likelihood is approximately Gaussian, the value of $-2\ln\Lambda(\boldsymbol{\alpha})$ follows a χ^2 distribution with a number of degrees of freedom n equal to the dimensionality of the vector $\boldsymbol{\alpha}$ [128]. This property is assumed to hold for all the results presented in the following sections. Confidence intervals for a confidence level (CL) $1 - p$ are then defined as the regions with values of $-2\ln\Lambda(\boldsymbol{\alpha})$ below a threshold $F_{\chi_n^2}^{-1}(1 - p)$, where $F_{\chi_n^2}^{-1}$ is the quantile function of the χ^2 distribution with n degrees of freedom. The CL_s prescription [129] is applied when setting an upper limits on a single parameter directly related to measured event rates, for instance a production cross section. When setting limits in more than one dimension, the CL_s procedure is not applied.

For relevant parameters of interest, a physical bound on the parameter values is included in the statistical interpretation. For example, branching fraction parameters cannot conceptually be smaller than zero. The 95% confidence interval quoted for such parameters is then based on the profile likelihood ratio restricted to the allowed region of parameter space, using the $\tilde{t}_\mu$ test statistic of Ref. [128]. The confidence interval is defined by the standard χ^2 cutoff, which leads to some over-coverage near the boundaries.

Total uncertainties in the measurement parameters are in some cases broken down into separate components for theory uncertainties affecting the background processes, theory uncertainties affecting the Higgs boson signal production, experimental uncertainties including MC statistical uncertainties, and statistical uncertainties. Each uncertainty component is derived by fixing the associated nuisance parameters to their best-fit values $\hat{\boldsymbol{\theta}}$ in both the numerator and denominator of Λ, and computing again the uncertainty in the measurement parameters. This is done for each component in turn, following the order in which they are listed above. The uncertainty obtained at each step is then subtracted in quadrature from the uncertainty obtained in the previous step (in the first step, from the total uncertainty) to obtain the corresponding uncertainty component. The statistical uncertainty component is obtained in the last step, with all nuisance parameters fixed except for the ones that are solely constrained by data, such as parameters used to describe data-driven background estimates.

The level of compatibility with the Standard Model is quantified using the test statistic

$$\lambda_{\text{SM}} = -2 \ln \Lambda(\alpha = \alpha_{\text{SM}}),$$

where α_{SM} are the Standard Model values of the parameters of interest. A p-value[3] p_{SM} is computed in the asymptotic approximation as $p_{\text{SM}} = 1 - F_{\chi_n^2}(\lambda_{\text{SM}})$, with n equal to the number of free parameters of interest. For the cross-section and branching fraction measurements reported in this paper, this definition does not account for the uncertainties in the SM values used as reference and may therefore lead to an underestimate of the p-value.

Results for expected significances and limits are obtained using the Asimov dataset technique [128].

The correlation coefficients presented in this paper are constructed to be symmetric around the observed best-fit values of the parameters of interest using the second derivatives of the negative log-likelihood ratio. Hence, the correlation matrices shown are not fully representative of the observed asymmetric uncertainties in the measurements. While the reported information is sufficient to reinterpret the measurements in terms of other parameterizations of the parameters of interest, this provides only an approximation to the information contained in the full likelihood function. For this reason, results for a number of commonly used parameterizations are also provided in Sections 5 to 7.

5 Combined measurements of signal strength, production cross sections and branching ratios

5.1 Global signal strength

The global signal strength μ is determined following the procedures used for the measurements performed at $\sqrt{s} = 7$ and 8 TeV [9]. For a specific production mode i and decay final state f, the signal yield is expressed in terms of a single modifier μ_{if}, as the production cross section σ_i and the branching fraction B_f cannot be separately measured without further assumptions. The modifiers are defined as the ratios of the measured Higgs boson yields and their SM expectations, denoted by the superscript "SM",

$$\mu_{if} = \frac{\sigma_i}{\sigma_i^{\text{SM}}} \times \frac{B_f}{B_f^{\text{SM}}}. \tag{2}$$

The SM expectation by definition corresponds to $\mu_{if} = 1$. The uncertainties in the SM predictions are included as nuisance parameters in the measurement of the signal strength modifiers, following the methodology introduced in Section 4, where the procedures to decompose the uncertainties are also described.

In the model used in this section, all the μ_{if} are set to a global signal strength μ, describing a common scaling of the expected Higgs boson yield in all categories. Its measured value is

$$\mu = 1.06 \pm 0.07 = 1.06 \pm 0.04 \,(\text{stat.}) \ \pm 0.03 \,(\text{exp.}) \ ^{+0.05}_{-0.04} \,(\text{sig. th.}) \ \pm 0.02 \,(\text{bkg. th.})$$

where the total uncertainty is decomposed into components for statistical uncertainties, experimental systematic uncertainties, and theory uncertainties in signal and background modeling. The signal theory

---

[3] The p-value is defined as the probability to obtain a value of the test statistic that is at least as high as the observed value under the hypothesis that is being tested.

component includes uncertainties due to missing higher-order perturbative QCD and electroweak corrections in the MC simulation, uncertainties in PDF and α_s values, the treatment of the underlying event, the matching between the hard-scattering process and the parton shower, choice of hadronization models, and branching fraction uncertainties. The measurement is consistent with the SM prediction with a p-value of $p_{SM} = 40\%$, computed using the procedure defined in Section 4 with one degree of freedom. The value of $-2\ln\Lambda(\mu)$ as a function of μ is shown in Figure 1, for the full likelihood and the reduced ones with sets of nuisance parameters sequentially fixed to their best-fit values to obtain the components of the uncertainty, as detailed in Section 4.
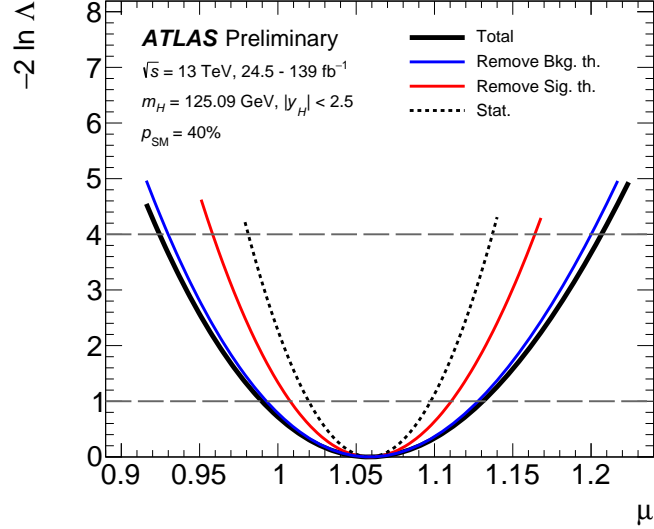
Figure 1: Variations of $-2\ln\Lambda(\mu)$ as a function of μ with all systematic uncertainties included (solid black line), with parameters describing theory uncertainties in background processes fixed to their best-fit values (solid blue line), with the same procedure also applied to theory uncertainties in the signal process (solid red line) and to all systematic uncertainties, so that only statistical uncertainties remain (dotted black line). The dashed horizontal lines show the levels $-2\ln\Lambda(\mu) = 1$ and $-2\ln\Lambda(\mu) = 4$ which are used to define, respectively, the 1σ and 2σ confidence intervals for μ. The level of compatibility between the measured global signal strength and the SM prediction corresponds to a p-value of $p_{SM} = 40\%$, computed using the procedure outlined in the text with one degree of freedom.

5.2 Production cross sections

Higgs boson production is studied in each of its main production modes. The production mechanisms considered are ggF, VBF, WH, ZH (including $gg \rightarrow ZH$), and the combination of $t\bar{t}H$ and tH ($t\bar{t}H + tH$). The small contribution from $b\bar{b}H$ (of the order of 1%) is grouped with ggF. In cases where several processes are combined, the combination assumes the relative fractions of each component to be as in the SM within corresponding theory uncertainties. Cross sections are reported in the region $|y_H| < 2.5$ of the Higgs boson rapidity y_H. Results are obtained in a simultaneous fit to the data, with the cross sections of each production mechanism as parameters of interest. Higgs boson decay branching fractions are set to their SM values, within the uncertainties specified in Ref. [39]. The results are shown in Figure 2 and Table 2.
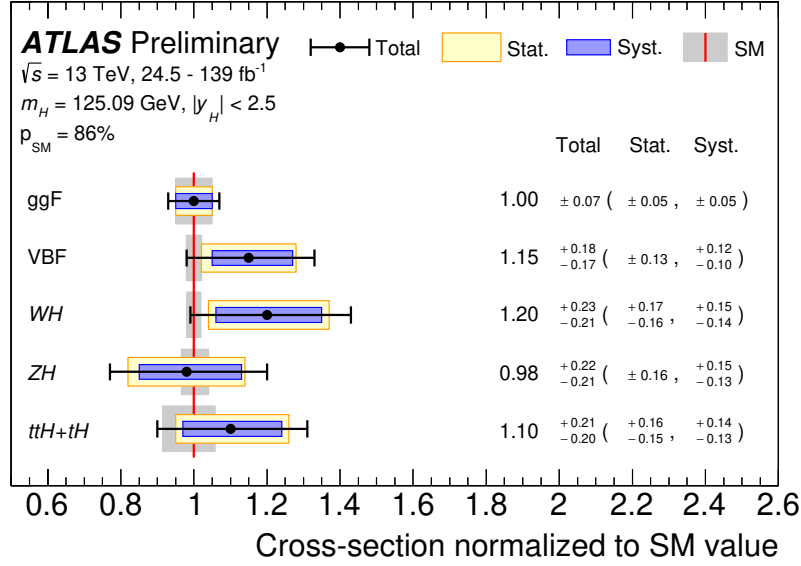
Figure 2: Cross sections for ggF, VBF, *WH*, *ZH* and $t\bar{t}H + tH$ normalized to their SM predictions, measured assuming SM values for the decay branching fractions. The black error bars, blue boxes and yellow boxes show the total, systematic, and statistical uncertainties in the measurements, respectively. The gray bands indicate the theory uncertainties in the SM cross-section predictions. The level of compatibility between the measurement and the SM prediction corresponds to a *p*-value of $p_{\text{SM}} = 86\%$, computed using the procedure outlined in the text with five degrees of freedom.

Table 2: Best-fit values and uncertainties for the production cross sections of the Higgs boson, assuming SM values for its decay branching fractions. The total uncertainties are decomposed into components for data statistics (Stat.) and systematic uncertainties (Syst.), and the systematic uncertainties are further decomposed into experimental (Exp.), signal theory (Sig. Th.) and background theory (Bkg. Th.) components. SM predictions are shown for the cross section of each production process. They are obtained from the inclusive cross-sections and associated uncertainties reported in Ref. [39], multiplied by an acceptance factor for the region $|y_H| < 2.5$ computed using the Higgs boson simulation samples described in Section 2.

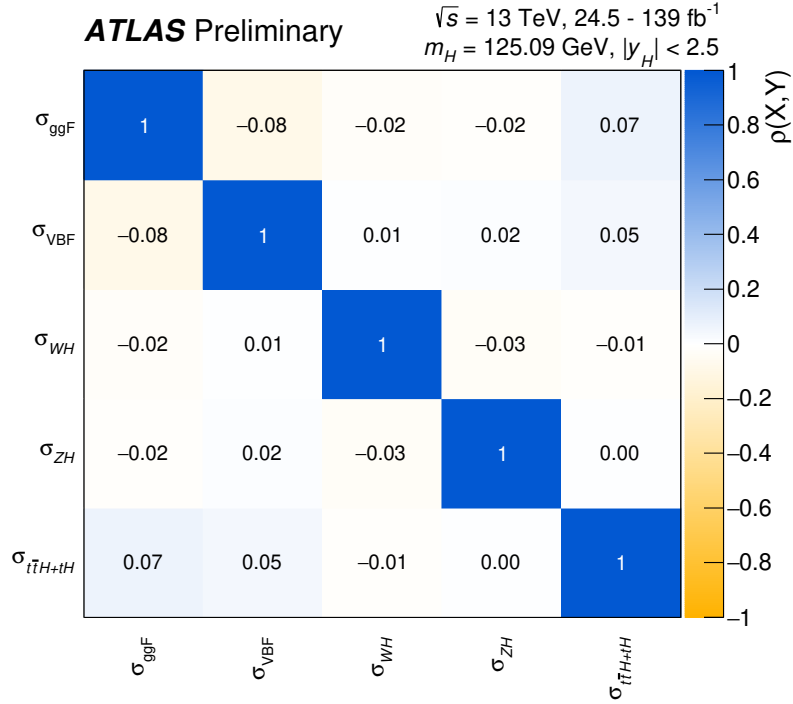| Process	Value	Uncertainty [pb]						SM pred.
($|y_H| < 2.5$)	[pb]	Total	Stat.	Syst.	Exp.	Sig. Th.	Bkg. Th.	[pb]
ggF	44.7	± 3.1	± 2.2	± 2.2	+ 1.8 − 1.7	+ 1.0 − 0.9	+ 0.9 − 0.7	44.7 ± 2.2
VBF	4.0	± 0.6	± 0.5	± 0.4	+ 0.3 − 0.2	± 0.3	± 0.1	$3.51 ^{+0.08}_{-0.07}$
WH	1.45	+ 0.28 − 0.25	+ 0.20 − 0.19	+ 0.18 − 0.17	+ 0.13 − 0.12	+ 0.08 − 0.06	+ 0.10 − 0.09	1.204 ± 0.024
ZH	0.78	+ 0.18 − 0.17	± 0.13	+ 0.12 − 0.10	+ 0.08 − 0.07	+ 0.07 − 0.05	± 0.06	$0.797 ^{+0.033}_{-0.026}$
$t\bar{t}H + tH$	0.64	± 0.12	± 0.09	± 0.08	+ 0.06 − 0.05	+ 0.03 − 0.02	± 0.05	$0.59 ^{+0.03}_{-0.05}$

Figure 3: Correlation matrix for the measurement of production cross sections of the Higgs boson, assuming SM values for its decay branching fractions.

The correlations between the measured cross sections, shown in Figure 3, are further reduced relative to previous analyses [21]. A modest correlation of -8% between the ggF and VBF processes remains, however, because of contributions from ggF production in the VBF-enriched selections. The level of compatibility between the measurement and the SM prediction corresponds to a p-value of $p_{\mathrm{SM}} = 86\%$, computed using the procedure outlined in Section 4 with five degrees of freedom.

Figure 4 shows the observed likelihood contours in the plane of σ_{ggF} versus σ_{VBF} from individual channels and the combined fit, together with the SM prediction. The cross sections for the other production modes are profiled, i.e. their values are determined by data as free parameters in the maximum likelihood fit, and the theory uncertainties on the predictions are assumed to be uncorrelated.

Significances relative to hypotheses in which individual production processes are absent are found to be above $5\,\sigma$ for all major production processes: ggF, VBF, WH, ZH, and $t\bar{t}H$+tH. For the WH and ZH modes, the observed (expected) significances are respectively $6.3\,\sigma$ ($5.2\,\sigma$) and $5.0\,\sigma$ ($5.4\,\sigma$) based on the asymptotic approximation, representing a first observation for the WH production mode.
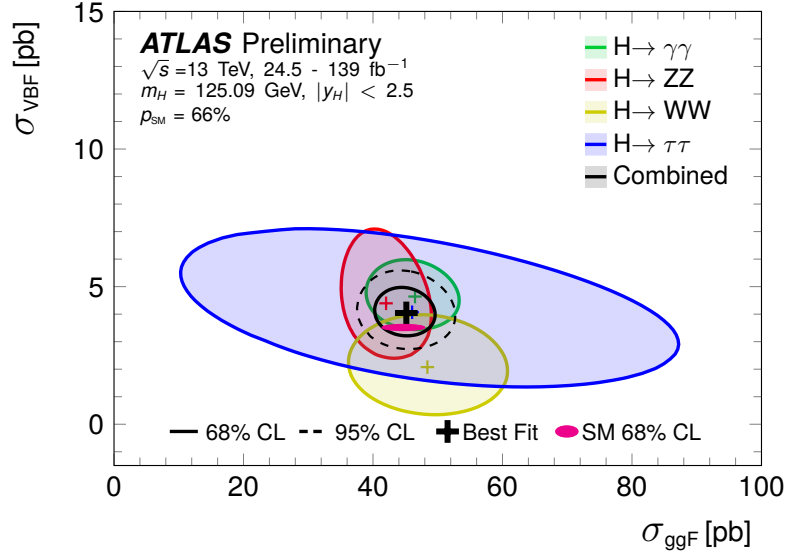
Figure 4: Observed likelihood contours in the plane of σ_{VBF} versus σ_{ggF} from individual channels and the combined fit. Contours for 68% CL, defined in the asymptotic approximation by $-2\ln\Lambda = 2.28$, are shown as solid lines. The 95% CL contour for the combined fit, corresponding to $-2\ln\Lambda = 5.99$, is also shown as a dashed line. The crosses indicate the best-fit values. The SM prediction is shown as a solid ellipse, produced by transforming the individual theory uncertainties on these processes into two-dimension by applying a scale factor of 1.51 obtained from the chi-squared quantile function, $\sqrt{F^{-1}_{\chi^2_2}(68\%)} = \sqrt{2.28}$. Higgs boson branching fractions are fixed to their SM values within theory uncertainties. The level of compatibility between the combined measurement and the SM prediction, estimated using the procedure outlined in the text with two degrees of freedom, corresponds to a p-value of $p_{\mathrm{SM}} = 66\%$.

5.3 Products of production cross sections and branching fractions

A description of both the production and decay mechanisms of the Higgs boson is obtained by considering the products $(\sigma \times B)_{if}$ of the cross section in production process i and branching fraction to final state f. The production processes are defined as in Section 5.2 except for the fact that the WH and ZH processes, which cannot be independently determined with the current $H \to ZZ^* \to \ell^+\ell^-\ell^+\ell^-$ analysis due to limited data statistics, are considered together as a single VH process, with the ratio of WH to ZH cross sections fixed to its SM value within uncertainties. The decay modes considered are $H \to \gamma\gamma$, $H \to ZZ^*$, $H \to WW^*$, $H \to \tau\tau$ and $H \to b\bar{b}$. There are in total 20 such independent products, but the analyses included in the combination provide little sensitivity to ggF production in the $H \to b\bar{b}$ decay mode, and to VH production in the $H \to WW^*$ and $H \to \tau\tau$ decay modes. The corresponding products are therefore fixed to their SM values within systematic uncertainties. The impact from fixing these processes to the SM is found to be negligible by comparing with an alternative parameterization where they are determined in the fit by assuming SM predicted relative fraction between $H \to WW^*$ and $H \to ZZ^*$, and between $H \to \tau\tau$ and $H \to b\bar{b}$. Also due to limited sensitivity, in $t\bar{t}H$ production the $H \to ZZ^*$ decay mode is considered together with $H \to WW^*$ as a single $H \to VV^*$ process, with the ratio of $H \to ZZ^*$ to $H \to WW^*$ fixed to its SM value. The results are obtained from a simultaneous fit of all input analyses, with the 16 independent $(\sigma \times B)$ products defined above as parameters of interest. They are shown in Figure 5 and Table 3. The correlation matrix of the measurements is shown in Figure 6. The largest correlations in absolute value are between the $t\bar{t}H$, $H \to VV^*$ and $t\bar{t}H$, $H \to \tau\tau$ processes, and between

the ggF, $H \to \tau\tau$ and VBF, $H \to \tau\tau$ processes. In both cases, this is due to cross-contamination between these processes in the analyses providing the most sensitive measurements. The level of compatibility between the measurement and the SM prediction corresponds to a p-value of $p_{\text{SM}} = 87\%$, computed using the procedure outlined in Section 4 with 16 degrees of freedom.

Table 3: Best-fit values and uncertainties for the production cross sections times branching fractions of the Higgs boson, for the combinations in which sufficient sensitivity is provided by the input analyses. Combinations not shown in the table are fixed to their SM values within uncertainties. For $t\bar{t}H + tH$ production, $H \to VV^*$ refers to the combination of $H \to WW^*$ and $H \to ZZ^*$, with a relative weight fixed by their respective SM branching fractions. The total uncertainties are decomposed into components for data statistics (Stat.) and systematic uncertainties (Syst.). SM predictions [39] are shown for each process.

| Process	Value	Uncertainty [fb]			SM pred.
($\lvert y_H \rvert < 2.5$)	[fb]	Total	Stat.	Syst.	[fb]
ggF, $H \to \gamma\gamma$	105	± 11	± 8	$^{+\,8}_{-\,7}$	101 ± 5
ggF, $H \to ZZ^*$	1110	$^{+\,130}_{-\,120}$	± 120	± 50	1180 ± 60
ggF, $H \to WW^*$	10400	$^{+\,1800}_{-\,1700}$	± 1100	± 1400	9600 ± 500
ggF, $H \to \tau\tau$	2900	$^{+\,1700}_{-\,1500}$	± 1100	$^{+\,1300}_{-\,1100}$	2800 ± 140
VBF, $H \to \gamma\gamma$	10.5	$^{+\,2.1}_{-\,1.8}$	$^{+\,1.5}_{-\,1.4}$	$^{+\,1.4}_{-\,1.2}$	7.98 ± 0.21
VBF, $H \to ZZ^*$	120	$^{+\,50}_{-\,40}$	± 40	± 10	92.8 ± 2.3
VBF, $H \to WW^*$	450	$^{+\,270}_{-\,260}$	$^{+\,220}_{-\,200}$	± 160	756 ± 19
VBF, $H \to \tau\tau$	250	$^{+\,130}_{-\,120}$	± 90	$^{+\,90}_{-\,80}$	220 ± 6
VBF, $H \to b\bar{b}$	6200	$^{+\,3400}_{-\,3300}$	± 3300	$^{+\,800}_{-\,500}$	2040 ± 50
$VH, H \to \gamma\gamma$	6.0	$^{+\,1.5}_{-\,1.4}$	$^{+\,1.4}_{-\,1.3}$	$^{+\,0.5}_{-\,0.4}$	$4.54\ ^{+\,0.13}_{-\,0.12}$
$VH, H \to ZZ^*$	80	$^{+\,60}_{-\,50}$	$^{+\,60}_{-\,50}$	± 10	52.8 ± 1.4
$VH, H \to b\bar{b}$	1190	$^{+\,210}_{-\,200}$	± 130	$^{+\,160}_{-\,140}$	$1162\ ^{+\,31}_{-\,29}$
$t\bar{t}H + tH, H \to \gamma\gamma$	1.20	$^{+\,0.36}_{-\,0.32}$	$^{+\,0.33}_{-\,0.31}$	$^{+\,0.12}_{-\,0.08}$	$1.33\ ^{+\,0.08}_{-\,0.12}$
$t\bar{t}H + tH, H \to VV^*$	240	± 80	± 60	± 50	$142\ ^{+\,9}_{-\,12}$
$t\bar{t}H + tH, H \to \tau\tau$	40	$^{+\,40}_{-\,30}$	± 30	$^{+\,30}_{-\,20}$	$36.7\ ^{+\,2.2}_{-\,3.2}$
$t\bar{t}H + tH, H \to b\bar{b}$	270	± 200	± 100	$^{+\,180}_{-\,170}$	$340\ ^{+\,20}_{-\,30}$
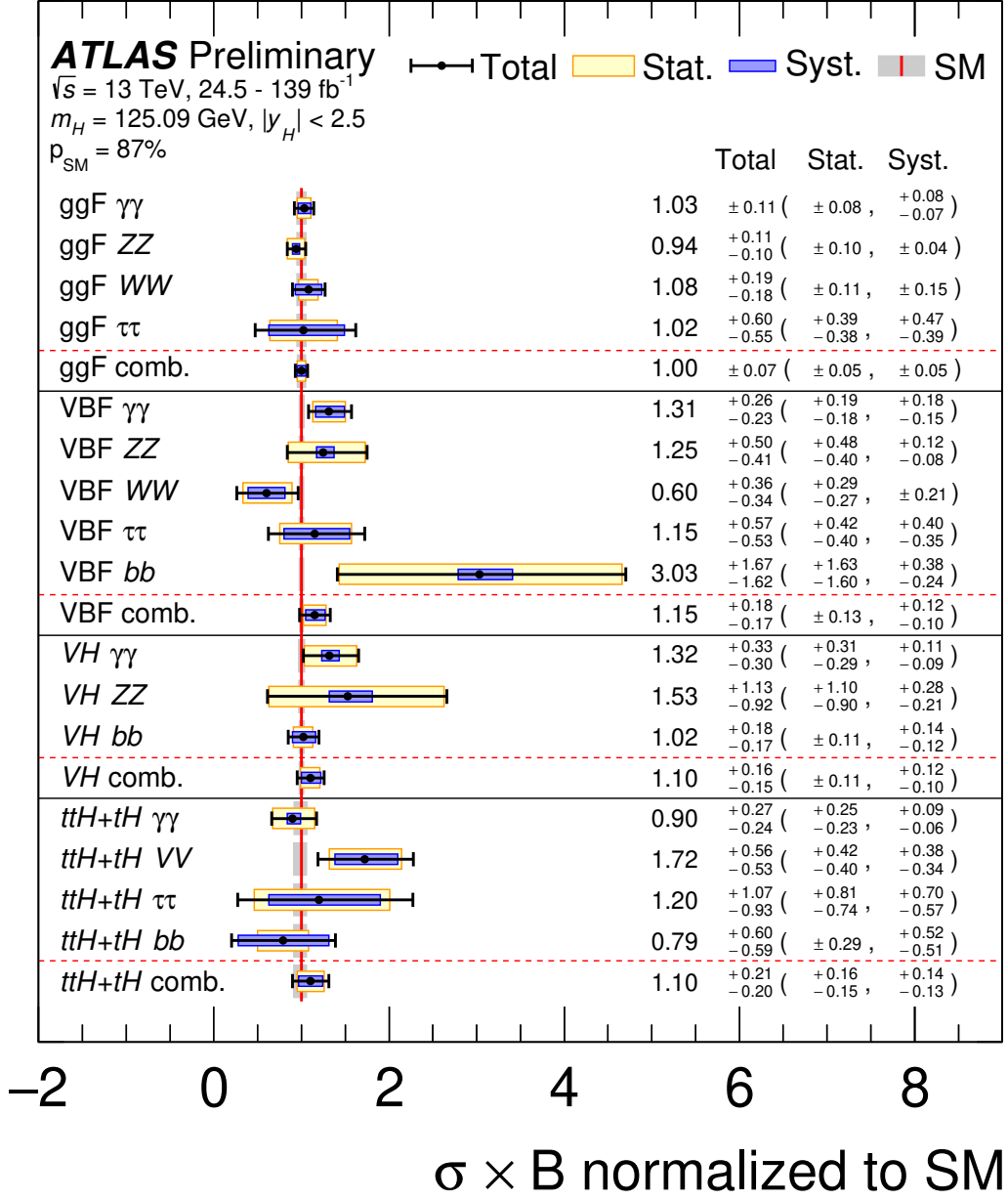
Figure 5: Cross sections times branching fraction for ggF, VBF, VH and $t\bar{t}H + tH$ production in each relevant decay mode, normalized to their SM predictions. The values are obtained from a simultaneous fit to all channels. The cross sections of the ggF, $H \to b\bar{b}$, $VH, H \to WW^*$ and $VH, H \to \tau\tau$ processes are fixed to their SM predictions. Combined results for each production mode are also shown, assuming SM values for the branching fractions into each decay mode. The black error bars, blue boxes and yellow boxes show the total, systematic, and statistical uncertainties in the measurements, respectively. The gray bands show the theory uncertainties in the predictions. The level of compatibility between the measurement and the SM prediction corresponds to a p-value of $p_{SM} = 87\%$, computed using the procedure outlined in the text with 16 degrees of freedom.
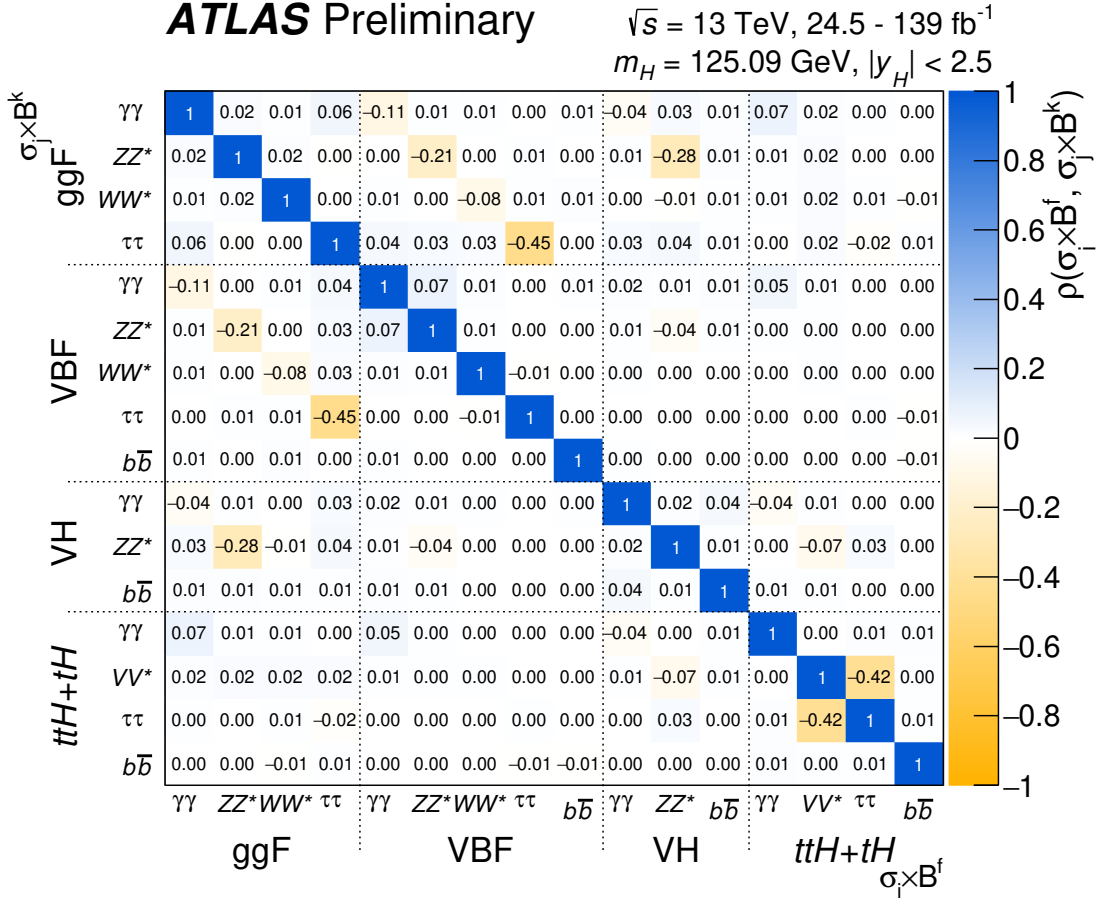
Figure 6: Correlation matrix for the measured values of the production cross sections times branching fractions of the Higgs boson, for the combinations in which sufficient sensitivity is provided by the input analyses.

5.4 Ratios of cross sections and branching fractions

The products $(\sigma \times B)_{if}$ described in Section 5.3 can be expressed as

$$(\sigma \times B)_{if} = \sigma_{\text{ggF}}^{ZZ} \cdot \left(\frac{\sigma_i}{\sigma_{\text{ggF}}}\right) \cdot \left(\frac{B_f}{B_{ZZ}}\right),$$

in terms of the cross section times branching fraction σ_{ggF}^{ZZ} for the reference process $gg \to H \to ZZ^*$, which is precisely measured and exhibits small systematic uncertainties, ratios of production cross sections to that of ggF, $\sigma_i/\sigma_{\text{ggF}}$, and ratios of branching fractions to that of $H \to ZZ^*$, B_f/B_{ZZ}.

Results are shown in Figure 7 and Table 4. The level of compatibility between the measurements and the SM predictions corresponds to a p-value of $p_{\text{SM}} = 97\%$, computed using the procedure outlined in Section 4 with nine degrees of freedom.
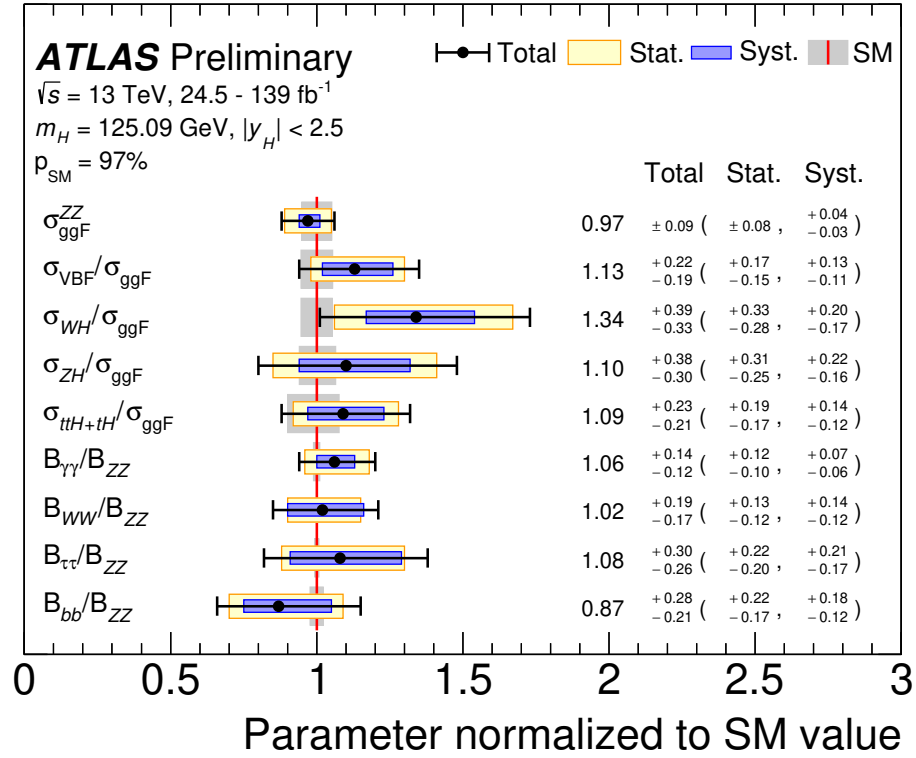
Figure 7: Results of a simultaneous fit for σ_{ggF}^{ZZ}, $\sigma_{VBF}/\sigma_{ggF}$, σ_{WH}/σ_{ggF}, σ_{ZH}/σ_{ggF}, $\sigma_{t\bar{t}H+tH}/\sigma_{ggF}$, $B_{\gamma\gamma}/B_{ZZ}$, B_{WW}/B_{ZZ}, $B_{\tau\tau}/B_{ZZ}$, and B_{bb}/B_{ZZ}. The fit results are normalized to the SM predictions. The black error bars, blue boxes and yellow boxes show the total, systematic, and statistical uncertainties in the measurements, respectively. The gray bands show the theory uncertainties in the predictions. The level of compatibility between the measurement and the SM prediction corresponds to a p-value of $p_{SM} = 97\%$, computed using the procedure outlined in the text with nine degrees of freedom.

Table 4: Best-fit values and uncertainties for $\sigma_{\mathrm{ggF}}^{ZZ}$, together with ratios of production cross sections divided by σ_{ggF}, and ratios of branching fractions divided by B_{ZZ}. The total uncertainties are decomposed into components for data statistics (Stat.) and systematic uncertainties (Syst.). The SM predictions [39] are also shown with their total uncertainties.

Quantity		Value	Uncertainty			SM prediction
			Total	Stat.	Syst.	
$\sigma_{\mathrm{ggF}}^{ZZ}$	[pb]	1.15	$\pm\,0.11$	$\pm\,0.09$	$+\,0.05 \atop -\,0.04$	1.18 ± 0.06
$\sigma_{\mathrm{VBF}}/\sigma_{\mathrm{ggF}}$		0.089	$+\,0.017 \atop -\,0.015$	$+\,0.013 \atop -\,0.012$	$+\,0.010 \atop -\,0.009$	0.079 ± 0.004
$\sigma_{WH}/\sigma_{\mathrm{ggF}}$		0.036	$+\,0.011 \atop -\,0.009$	$+\,0.009 \atop -\,0.008$	$\pm\,0.005$	$0.0269 \; {+\,0.0014 \atop -\,0.0015}$
$\sigma_{ZH}/\sigma_{\mathrm{ggF}}$		0.020	$+\,0.007 \atop -\,0.005$	$+\,0.006 \atop -\,0.004$	$+\,0.004 \atop -\,0.003$	$0.0178 \; {+\,0.0011 \atop -\,0.0010}$
$\sigma_{t\bar{t}H+tH}/\sigma_{\mathrm{ggF}}$		0.0143	$+\,0.0030 \atop -\,0.0028$	$+\,0.0025 \atop -\,0.0022$	$+\,0.0018 \atop -\,0.0016$	$0.0131 \; {+\,0.0010 \atop -\,0.0013}$
$B_{\gamma\gamma}/B_{ZZ}$		0.091	$+\,0.012 \atop -\,0.010$	$+\,0.010 \atop -\,0.009$	$+\,0.006 \atop -\,0.005$	0.0860 ± 0.0010
B_{WW}/B_{ZZ}		8.3	$+\,1.5 \atop -\,1.4$	$+\,1.1 \atop -\,1.0$	$+\,1.1 \atop -\,1.0$	$8.15 \pm\, <0.01$
$B_{\tau\tau}/B_{ZZ}$		2.6	$+\,0.7 \atop -\,0.6$	$\pm\,0.5$	$+\,0.5 \atop -\,0.4$	2.369 ± 0.017
B_{bb}/B_{ZZ}		19	$+\,6 \atop -\,5$	$+\,5 \atop -\,4$	$+\,4 \atop -\,3$	22.0 ± 0.5

6 Combined measurements of simplified template cross sections

6.1 Simplified template cross-section framework

Simplified template cross sections [39–42] are defined through a partition of the phase space of the SM Higgs production processes into a set of non-overlapping regions. These regions are defined in terms of the kinematics of the Higgs boson and, when they are present, of associated jets and W and Z bosons, independently of the Higgs boson decay process. They are chosen according to three criteria: sensitivity to deviations from the SM expectation, avoidance of large theory uncertainties in the corresponding SM predictions, and to approximately match experimental selections so as to minimize model-dependent extrapolations. Analysis selections do not, however, necessarily correspond exactly to the STXS regions.

All regions are defined for a Higgs boson rapidity y_H satisfying $|y_H| < 2.5$, corresponding approximately to the region of experimental sensitivity. Jets are reconstructed from all stable particles with a lifetime greater than 10 ps, excluding the decay products of the Higgs boson and leptons from W and Z boson decays, using the anti-k_t algorithm with a jet radius parameter $R = 0.4$, and must have a transverse momentum $p_{T,jet} > 30$ GeV.

The measurements presented in this paper use the regions of phase space specified by the Stage 1.2 splitting of the STXS framework. Higgs boson production is first classified according to the nature of the initial state and the associated particles, the latter including the decay products of the W and Z bosons if they are present. These classes are: $t\bar{t}H$ and tH processes; $qq \rightarrow Hqq$ processes, with contributions from both VBF production and quark-initiated VH production with a hadronic decay of the gauge boson; VH production with a leptonic decay of the vector boson ($V(\text{lep})H$), including $gg \rightarrow ZH$ production; and finally the ggF process. The last is considered together with $gg \rightarrow ZH$, $Z \rightarrow q\bar{q}$ production, as a single $gg \rightarrow H$ process. The $b\bar{b}H$ production mode is modeled as a 1% [39] increase of the $gg \rightarrow H$ yield in each STXS bin, since the acceptances for both processes are similar for all input analyses [39].

The input analyses included in this paper provide only limited sensitivity to the cross section in some bins of the Stage 1.2 scheme, mainly because of the small number of events in some regions. In other cases, they only provide sensitivity to a combination of bins, leading to strongly correlated measurements. To mitigate these effects, some of the bins as defined in Stage 1.2 have been merged for this combined analysis. These measurement bins are defined as follows for each process, and summarized in Figure 8:

- **$gg \rightarrow H$** is separated into regions defined by the jet multiplicity, the Higgs boson transverse momentum p_T^H, and in case there are at least two jets the invariant mass of the two leading jets m_{jj}. A region is defined for events with $p_T^H \geq 200$ GeV, providing sensitivity to deviations from the SM at high momentum transfer. This region is further partitioned into three p_T^H bins: $200 - 300$ GeV, $300 - 450$ GeV and ≥ 450 GeV. The remaining events are separated into regions with 0, 1 and ≥ 2 jets in the final state. The 0-jet and 1-jet regions are further split into bins of p_T^H, probing perturbative QCD predictions and providing sensitivity to deviations from the SM. Two bins are defined with p_T^H below and above 10 GeV in the 0-jet region, and three p_T^H bins are defined for < 60 GeV, $60 - 120$ GeV and $120 - 200$ GeV in the 1-jet region. As for the 2-jet region, it is first divided into two regions with m_{jj} below and above 350 GeV. The former is then further divided into two p_T^H bins: < 120 GeV and $120 - 200$ GeV.

- **$qq \rightarrow Hqq$** is separated into ≤ 1-jet and ≥ 2-jet regions. The ≥ 2-jet region is then divided into two regions, namely m_{jj} below and above 350 GeV. The $m_{jj} < 350$ GeV region is further split into two

bins, one with m_{jj} in 60 – 120 GeV, which include a large fraction of VH events with hadronically decaying vector bosons (VH topo). The other bin contains the remaining events with m_{jj} in the range of either < 60 GeV or 120 – 350 GeV (VH veto). The $m_{jj} \geq 350$ GeV region is separated into two p_T^H regions below and above 200 GeV. The latter is further divided into two bins with m_{jj} in 350 – 700 GeV and above 700 GeV.

- **V(lep)H** is split into the two processes $qq \rightarrow WH$ and $pp \rightarrow ZH$, the latter including both quark-initiated and gluon-initiated productions. These regions are further split according to p_T^V, the transverse momentum of the W or Z boson. For the $qq \rightarrow WH$ process four bins are defined for p_T^V: < 75 GeV, 75 – 150 GeV, 150 – 250 GeV and ≥ 250 GeV, while for $pp \rightarrow ZH$ three bins are defined for p_T^V: < 150 GeV, 150 – 250 GeV and ≥ 250 GeV.

- **$t\bar{t}H$** is split into four p_T^H bins defined as < 60 GeV, 60 – 120 GeV, 120 – 200 GeV and ≥ 200 GeV. **tH** is a single bin in the measurement.

The measured event yields are described by Eq. (1), with parameters of interest of the form $(\sigma \times B)_{if}$ denoting the cross section times branching fraction in STXS region i and decay channel f. The acceptance factors $(\epsilon \times A)_{if}^k$ for each analysis region k are determined from SM Higgs boson production processes, modeled using the samples described in Section 2, and act as templates in the fits of the STXS cross sections to the data. The dependence on the theory assumptions is less than in the measurement of the total cross sections in each production mode, since the $(\epsilon \times A)_{if}^k$ are computed over smaller regions. Assumptions about the kinematics within a given STXS region lead to some model-dependence, which can be reduced further by using a finer splitting of the phase space, as allowed by experimental precision in the future. As for the other results reported in this note, the STXS measurements assume the SM predictions for Higgs boson decays. BSM scenarios such as those described in Ref. [11] can significantly modify the acceptance of the signal, in particular for the WW^* or ZZ^* decay channels, which should be considered when using these measurements for the relevant interpretations.

Theory uncertainties for the $gg \rightarrow H$, $qq \rightarrow Hqq$, and $t\bar{t}H$ processes are defined as in Ref. [10, 11], while those of the $V(\text{lep})H$ process follow the scheme described in Ref. [130]. For the measurement bins defined by merging several bins of the STXS Stage-1.2 framework, the $(\epsilon \times A)$ factors are determined assuming that the relative fractions of each Stage-1.2 bin are as in the SM, and SM uncertainties in these fractions are taken into account.
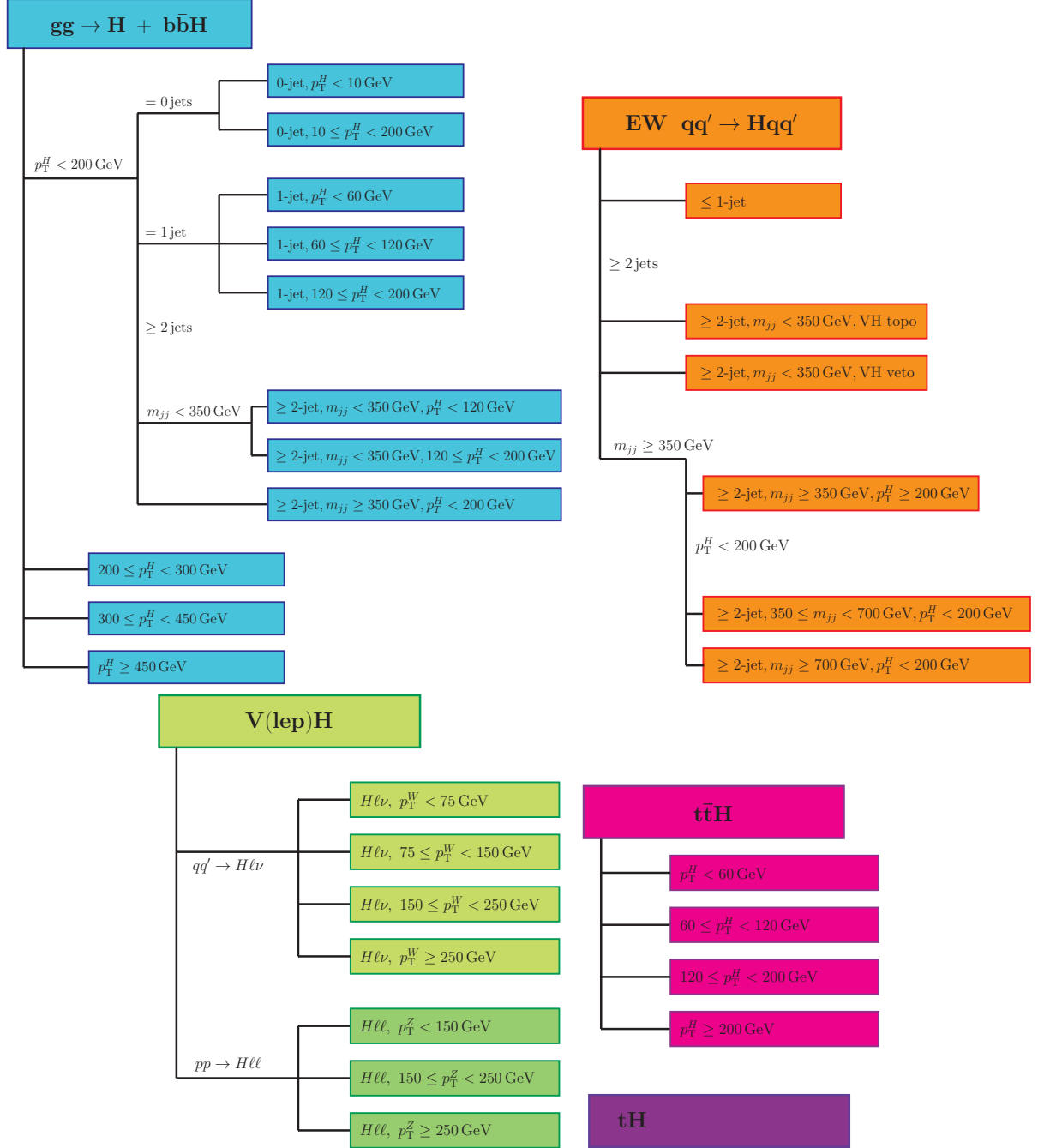
gg → H + bb̄H

= 0 jets
- 0-jet, $p_T^H < 10$ GeV
- 0-jet, $10 \leq p_T^H < 200$ GeV

$p_T^H < 200$ GeV

= 1 jet
- 1-jet, $p_T^H < 60$ GeV
- 1-jet, $60 \leq p_T^H < 120$ GeV
- 1-jet, $120 \leq p_T^H < 200$ GeV

≥ 2 jets

$m_{jj} < 350$ GeV
- ≥ 2-jet, $m_{jj} < 350$ GeV, $p_T^H < 120$ GeV
- ≥ 2-jet, $m_{jj} < 350$ GeV, $120 \leq p_T^H < 200$ GeV
- ≥ 2-jet, $m_{jj} \geq 350$ GeV, $p_T^H < 200$ GeV

- $200 \leq p_T^H < 300$ GeV
- $300 \leq p_T^H < 450$ GeV
- $p_T^H \geq 450$ GeV

EW qq′ → Hqq′

- ≤ 1-jet

≥ 2 jets

- ≥ 2-jet, $m_{jj} < 350$ GeV, VH topo
- ≥ 2-jet, $m_{jj} < 350$ GeV, VH veto

$m_{jj} \geq 350$ GeV

- ≥ 2-jet, $m_{jj} \geq 350$ GeV, $p_T^H \geq 200$ GeV

$p_T^H < 200$ GeV

- ≥ 2-jet, $350 \leq m_{jj} < 700$ GeV, $p_T^H < 200$ GeV
- ≥ 2-jet, $m_{jj} \geq 700$ GeV, $p_T^H < 200$ GeV

V(lep)H

$qq′ → H\ell\nu$
- $H\ell\nu$, $p_T^W < 75$ GeV
- $H\ell\nu$, $75 \leq p_T^W < 150$ GeV
- $H\ell\nu$, $150 \leq p_T^W < 250$ GeV
- $H\ell\nu$, $p_T^W \geq 250$ GeV

$pp → H\ell\ell$
- $H\ell\ell$, $p_T^Z < 150$ GeV
- $H\ell\ell$, $150 \leq p_T^Z < 250$ GeV
- $H\ell\ell$, $p_T^Z \geq 250$ GeV

tt̄H

- $p_T^H < 60$ GeV
- $60 \leq p_T^H < 120$ GeV
- $120 \leq p_T^H < 200$ GeV
- $p_T^H \geq 200$ GeV

tH

Figure 8: Definition of the STXS measurement regions used in this note.

22

6.2 Results

The fit parameters chosen for the combined STXS measurements are the cross sections for Higgs boson production in STXS region i times the branching fraction for the $H \rightarrow ZZ^*$ decay, $(\sigma \times B)_{i,ZZ}$, and the ratios of branching fractions B_f/B_{ZZ} for the other final states f. Similarly to the ratio model in Section 5.4, the cross sections times branching fractions for final states other than ZZ are parameterized as

$$(\sigma \times B)_{if} = (\sigma \times B)_{i,ZZ} \cdot \left(\frac{B_f}{B_{ZZ}} \right).$$

The results are shown in Figure 9 and Table 5. The observed (expected) upper limit at 95% CL on the tH cross section is 8.4 (8.2) times the SM prediction.

The results are in agreement with the SM predictions within uncertainties in a wide range of kinematic regions for the different Higgs boson production processes. The level of compatibility between the measurement and the SM prediction corresponds to a p-value of $p_{SM} = 95\%$, computed using the procedure outlined in Section 4 with 31 degrees of freedom.
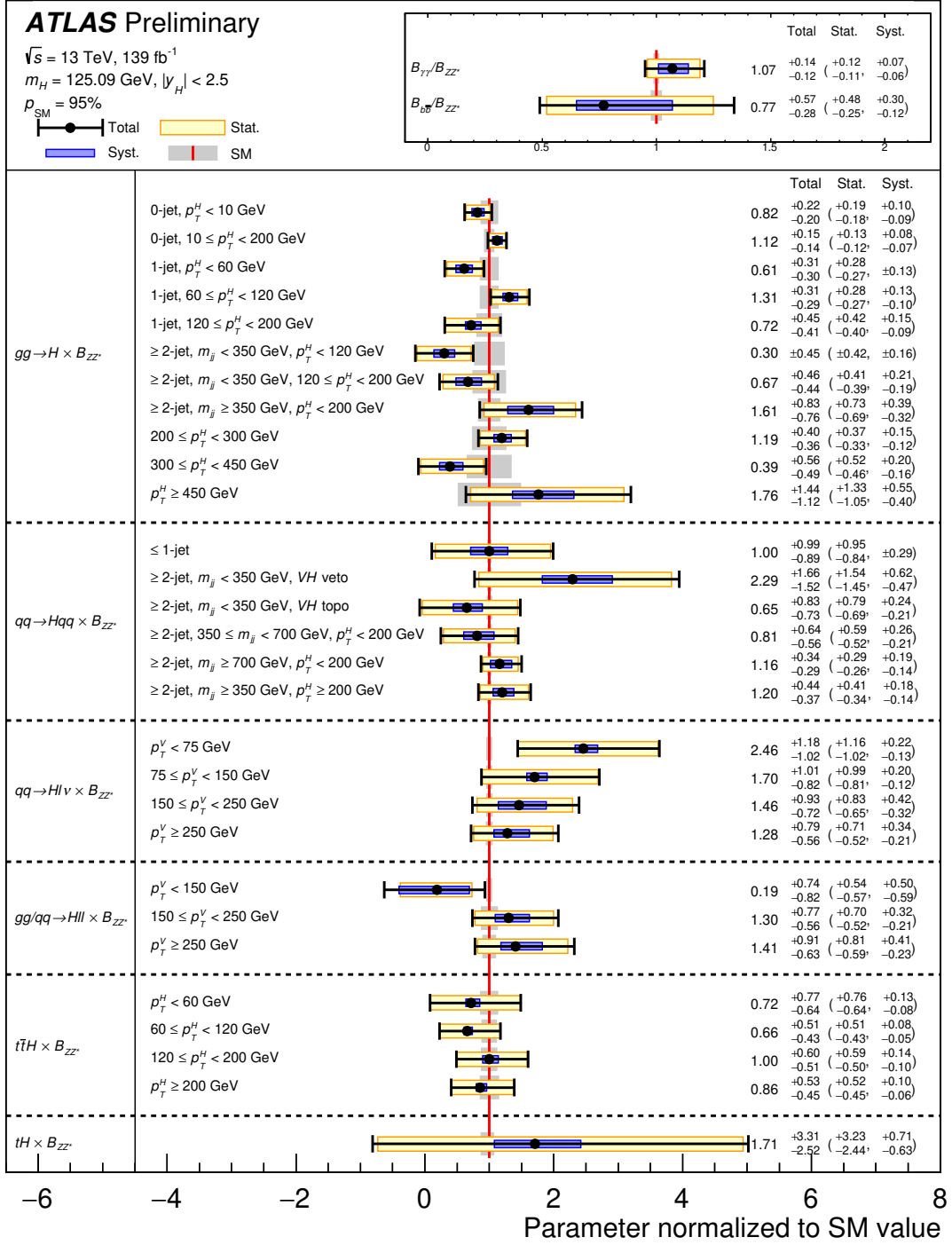
Figure 9: Best-fit values and uncertainties for the cross sections in each measurement region and of the ratios of branching fractions B_f/B_{ZZ}, normalized to the SM predictions for the various parameters. The parameters directly extracted from the fit are the products ($\sigma_i \times B_{ZZ}$) and the ratios B_f/B_{ZZ}. The black error bar shows the total uncertainty in each measurement. The level of compatibility between the combined measurement and the SM prediction, estimated using the procedure outlined in the text with 31 degrees of freedom, corresponds to a p-value of $p_{SM} = 95\%$.
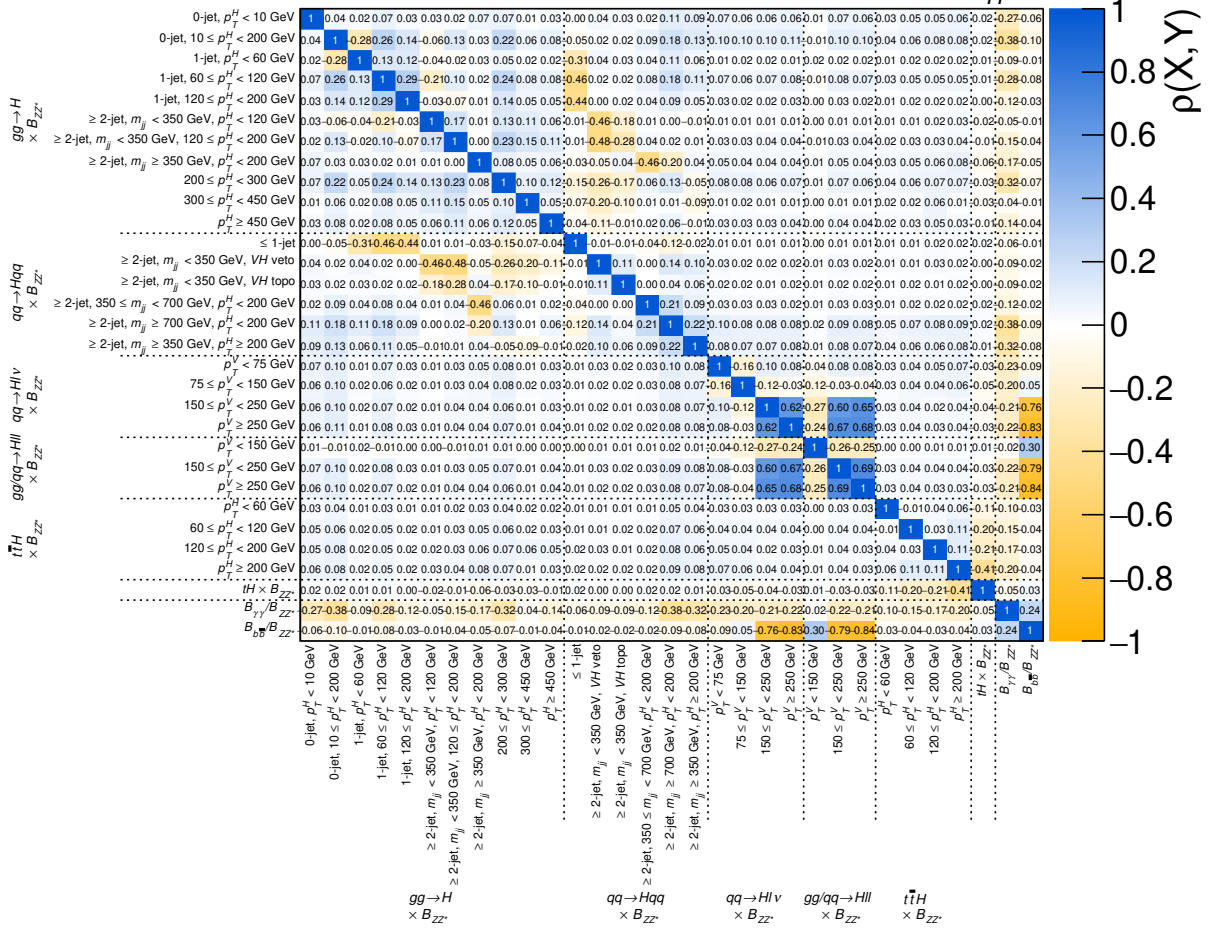
Figure 10: Correlation matrix for the measured values of the simplified template cross sections and ratios of branching fractions. The fit parameters are the products $(\sigma_i \times B_{ZZ})$ and the ratios B_f / B_{ZZ}.

Table 5: Best-fit values and uncertainties for the cross sections in each measurement region, and of the ratios of branching fractions B_f/B_{ZZ}. The total uncertainties are decomposed into components for data statistics (Stat.) and systematic uncertainties (Syst.). The SM predictions [39] are also shown for each quantity with their total uncertainties. The parameters directly extracted from the fit are the products $(\sigma_i \times B_{ZZ})$ and the ratios B_f/B_{ZZ}; the former are shown divided by the SM value of B_{ZZ}.

Measurement region $\left((\sigma_i \times B_{ZZ})/B_{ZZ}^{\text{SM}}\right)$	Value [pb]	Uncertainty [pb] Total	Stat.	Syst.	SM prediction [pb]
$gg \to H$, $0-$jet, $p_T^H < 10\,\text{GeV}$	5.5	$+1.5$ -1.3	$+1.3$ -1.2	$+0.7$ -0.6	6.7 ± 0.9
$gg \to H$, $0-$jet, $10 \le p_T^H < 200\,\text{GeV}$	23.3	$+3.1$ -2.9	$+2.7$ -2.5	$+1.7$ -1.5	20.8 ± 1.6
$gg \to H$, $1-$jet, $p_T^H < 60\,\text{GeV}$	4.0	± 2.0	± 1.8	± 0.9	6.6 ± 0.9
$gg \to H$, $1-$jet, $60 \le p_T^H < 120\,\text{GeV}$	6.0	$+1.4$ -1.3	$+1.3$ -1.2	$+0.6$ -0.5	4.5 ± 0.6
$gg \to H$, $1-$jet, $120 \le p_T^H < 200\,\text{GeV}$	0.54	$+0.34$ -0.31	$+0.32$ -0.30	$+0.11$ -0.07	0.75 ± 0.15
$gg \to H$, $\ge 2-$jet, $m_{jj} < 350\,\text{GeV}$, $p_T^H < 120\,\text{GeV}$	0.9	± 1.3	± 1.3	± 0.5	3.0 ± 0.7
$gg \to H$, $\ge 2-$jet, $m_{jj} < 350\,\text{GeV}$, $120 \le p_T^H < 200\,\text{GeV}$	0.6	± 0.4	± 0.4	± 0.2	0.95 ± 0.24
$gg \to H$, $\ge 2-$jet, $m_{jj} \ge 350\,\text{GeV}$, $p_T^H < 200\,\text{GeV}$	1.4	± 0.7	± 0.6	± 0.3	0.88 ± 0.15
$gg \to H$, $200 \le p_T^H < 300\,\text{GeV}$	0.55	$+0.18$ -0.17	$+0.17$ -0.15	$+0.07$ -0.06	0.46 ± 0.12
$gg \to H$, $300 \le p_T^H < 450\,\text{GeV}$	0.04	$+0.06$ -0.05	$+0.06$ -0.05	± 0.02	0.11 ± 0.04
$gg \to H$, $p_T^H \ge 450\,\text{GeV}$	0.031	$+0.026$ -0.020	$+0.024$ -0.019	$+0.010$ -0.007	0.018 ± 0.009
$qq \to Hqq$, $\le 1-$jet	2.1	$+2.1$ -1.9	$+2.0$ -1.8	± 0.6	2.10 ± 0.06
$qq \to Hqq$, $\ge 2-$jet, $m_{jj} < 350\,\text{GeV}$, VH veto	1.7	$+1.2$ -1.1	± 1.1	$+0.5$ -0.3	0.728 ± 0.022
$qq \to Hqq$, $\ge 2-$jet, $m_{jj} < 350\,\text{GeV}$, VH topo	0.3	± 0.4	± 0.4	± 0.1	$0.527 \,{}^{+0.019}_{-0.020}$
$qq \to Hqq$, $\ge 2-$jet, $350 \le m_{jj} < 700\,\text{GeV}$, $p_T^H < 200\,\text{GeV}$	0.44	$+0.35$ -0.31	$+0.32$ -0.28	$+0.14$ -0.11	0.545 ± 0.016
$qq \to Hqq$, $\ge 2-$jet, $m_{jj} \ge 700\,\text{GeV}$, $p_T^H < 200\,\text{GeV}$	0.85	$+0.25$ -0.21	$+0.21$ -0.19	$+0.14$ -0.10	0.735 ± 0.022
$qq \to Hqq$, $\ge 2-$jet, $m_{jj} \ge 350\,\text{GeV}$, $p_T^H \ge 200\,\text{GeV}$	0.19	$+0.07$ -0.06	$+0.07$ -0.05	$+0.03$ -0.02	0.160 ± 0.004
$qq \to H\ell\nu$, $p_T^V < 75\,\text{GeV}$	0.51	$+0.24$ -0.21	$+0.24$ -0.21	$+0.05$ -0.03	0.206 ± 0.008
$qq \to H\ell\nu$, $75 \le p_T^V < 150\,\text{GeV}$	0.22	$+0.13$ -0.11	$+0.13$ -0.11	$+0.03$ -0.02	$0.131 \,{}^{+0.005}_{-0.006}$
$qq \to H\ell\nu$, $150 \le p_T^V < 250\,\text{GeV}$	0.06	$+0.04$ -0.03	± 0.03	$+0.02$ -0.01	0.0414 ± 0.0018
$qq \to H\ell\nu$, $p_T^V \ge 250\,\text{GeV}$	0.017	$+0.011$ -0.008	$+0.010$ -0.007	$+0.005$ -0.003	0.0134 ± 0.0006
$gg/qq \to H\ell\ell$, $p_T^V < 150\,\text{GeV}$	0.04	$+0.15$ -0.16	± 0.11	$+0.10$ -0.12	0.197 ± 0.008
$gg/qq \to H\ell\ell$, $150 \le p_T^V < 250\,\text{GeV}$	0.042	$+0.025$ -0.018	$+0.022$ -0.017	$+0.010$ -0.007	0.032 ± 0.004
$gg/qq \to H\ell\ell$, $p_T^V \ge 250\,\text{GeV}$	0.012	$+0.008$ -0.005	$+0.007$ -0.005	$+0.004$ -0.002	0.0087 ± 0.0009
$t\bar{t}H$, $p_T^H < 60\,\text{GeV}$	0.09	$+0.09$ -0.08	$+0.09$ -0.08	$+0.02$ -0.01	0.118 ± 0.016
$t\bar{t}H$, $60 \le p_T^H < 120\,\text{GeV}$	0.12	$+0.09$ -0.08	$+0.09$ -0.08	± 0.01	0.178 ± 0.020
$t\bar{t}H$, $120 \le p_T^H < 200\,\text{GeV}$	0.13	$+0.08$ -0.06	$+0.07$ -0.06	$+0.02$ -0.01	0.126 ± 0.015
$t\bar{t}H$, $p_T^H \ge 200\,\text{GeV}$	0.07	$+0.04$ -0.03	$+0.04$ -0.03	$+0.01$ -0.00	0.077 ± 0.011
tH	0.14	$+0.28$ -0.21	$+0.27$ -0.21	$+0.06$ -0.05	$0.085 \,{}^{+0.005}_{-0.011}$
Branching fraction ratio					
$B_{\gamma\gamma}/B_{ZZ}$	0.092	$+0.012$ -0.010	$+0.010$ -0.009	$+0.006$ -0.005	0.0860 ± 0.0010
$B_{b\bar{b}}/B_{ZZ}$	17	$+13$ -6	$+11$ -5	$+7$ -3	22.0 ± 0.5

7 Interpretation of results in the κ framework

When testing the Higgs boson coupling strengths, the production cross sections σ_i and decay branching fractions B_f defined in Eq. (2) cannot be treated independently, as they often involve the same Higgs boson coupling strengths. Scenarios with a consistent treatment of coupling strengths in Higgs boson production and decay modes are presented in this section.

7.1 Framework for coupling-strength measurements

Coupling-strength modifiers κ are introduced to study modifications of the Higgs boson couplings related to BSM physics, within a framework [43] (κ-framework) based on the leading-order contributions to each production and decay process. Within the assumptions made in this framework, the Higgs boson production and decay can be factorized, such that the cross section times branching fraction of an individual channel $\sigma(i \to H \to f)$ contributing to a measured signal yield is parameterized as

$$\sigma_i \times B_f = \frac{\sigma_i(\boldsymbol{\kappa}) \times \Gamma_f(\boldsymbol{\kappa})}{\Gamma_H}, \tag{3}$$

where Γ_H is the total width of the Higgs boson and Γ_f is the partial width for Higgs boson decay into the final state f. For a given production process or decay mode j, the corresponding coupling-strength modifier κ_j is defined by

$$\kappa_j^2 = \frac{\sigma_j}{\sigma_j^{\mathrm{SM}}} \quad \text{or} \quad \kappa_j^2 = \frac{\Gamma_j}{\Gamma_j^{\mathrm{SM}}}.$$

The SM expectation, denoted by the label "SM", by definition corresponds to $\kappa_j = 1$.

The total width of the Higgs boson is given by the sum of the partial widths for the decay modes included in the present measurements, and contributions from the following two additional classes of Higgs boson decays.

- Invisible decays: decays which are identified through an $E_{\mathrm{T}}^{\mathrm{miss}}$ signature in the analyses described in Section 3.5. In the SM, the branching fraction of invisible decays is predicted to be 0.1%, exclusively from the $H \to ZZ^* \to 4\nu$ process. The BSM contribution to this branching fraction is denoted as $B_{\mathrm{i.}}$.

- Undetected decays: decays to which none of the analyses included in this combination are sensitive, such as decays to light quarks which have not yet been resolved, or undetected BSM particles without a sizable $E_{\mathrm{T}}^{\mathrm{miss}}$ in the final state. For the former, the SM contribution of these undetected decays is already included in Γ^{SM}, and amounts to 11%, mainly driven by the decays to gluon pairs. The BSM contribution to the undetected branching fraction is denoted as $B_{\mathrm{u.}}$. Note that deviations of the partial width of the input measurements of this analysis are separately included by scaling their partial width by κ_j.

BSM contributions to the total Higgs boson decay width may manifest themselves as a value of κ_j differing from one, or a value of B_i or B_u differing from zero. The Higgs boson total width is then expressed as $\Gamma_H(\kappa, B_i, B_u) = \kappa_H^2(\kappa, B_i, B_u) \Gamma_H^{\text{SM}}$ with

$$\kappa_H^2(\kappa, B_i, B_u) = \frac{\sum_j B_j^{\text{SM}} \kappa_j^2}{(1 - B_i - B_u)}. \tag{4}$$

By definition, B_u is not directly constrained by any measurement, so that extracting values for both the kappa parameters and B_u simultaneously requires additional assumptions or constraints. In fact all the measured cross sections included in this combination would be left unchanged for certain choices of values for the κ parameters and B_u, as the changes would divide out in the ratio, as can be seen Eqs. (3) and (4). The simplest assumption is that there are no undetected Higgs boson decays and the invisible branching fraction is as predicted by the SM. An alternative, weaker assumption, is to require $\kappa_W \le 1$ and $\kappa_Z \le 1$ [43]. Another possible alternative, used in the previous combination [21] but not in the current note, is based on the measured signal strength of off-shell Higgs boson production to constrain the total Higgs width, assuming off-shell and on-shell coupling-strength scale factors are the same.

An alternative approach is to rely on measurements of ratios of coupling-strength scale factors, which can be measured without assumptions about the Higgs boson total width, since the dependence on Γ_H of each coupling strength cancels in their ratios [4].

The current LHC data are nearly insensitive to the coupling-strength modifiers κ_c and κ_s. Thus, in the following it is assumed that κ_c varies as κ_t and κ_s varies as κ_b. Other coupling modifiers (κ_u, κ_d, and κ_e) are irrelevant for the combination provided they are of order unity. The $gg \to H$, $H \to gg$, $gg \to ZH$, $H \to \gamma\gamma$, and $H \to Z\gamma$ processes are loop-induced in the SM. The ggH vertex and the $H \to \gamma\gamma$ process are treated either using effective scale factors κ_g and κ_γ, respectively, or expressed in terms of the more fundamental coupling-strength scale factors corresponding to the particles that contribute to the loop in the SM, including all interference effects. The $gg \to ZH$ process is never described using an effective scale factor and always resolved in terms of modifications of the SM Higgs boson couplings to the top quark and the Z boson. Similarly, the $H \to Z\gamma$ decay is always expressed in terms of the Higgs boson couplings to the W boson and the t-quark as no analysis targeting this decay mode is included in the combination. These relations are summarized in Table 6. All uncertainties in the best-fit values shown in the following take into account both the experimental and theoretical systematic uncertainties, following the procedures outlined in Section 4.

---

[4] For the validity of κ-framework the narrow-width assumption should still hold.

Table 6: Parametrizations of Higgs boson production cross sections σ_i, partial decay widths Γ^f, and the total width Γ_H, normalized to their SM values, as functions of the coupling-strength modifiers κ. The effect of invisible and undetected decays is not considered in the expression for Γ_H. For effective κ parameters associated with loop processes, the resolved scaling in terms of the modifications of the Higgs boson couplings to the fundamental SM particles is given. The coefficients are derived following the methodology in Ref. [39, 43].

Production	Loops	Main interference	Effective modifier	Resolved modifier
$\sigma(\text{ggF})$	✓	t–b	κ_g^2	$1.040\,\kappa_t^2 + 0.002\,\kappa_b^2 - 0.038\,\kappa_t\kappa_b - 0.005\,\kappa_t\kappa_c$
$\sigma(\text{VBF})$	-	-	-	$0.733\,\kappa_W^2 + 0.267\,\kappa_Z^2$
$\sigma(qq/qg \to ZH)$	-	-	-	κ_Z^2
$\sigma(gg \to ZH)$	✓	t–Z	$\kappa_{(ggZH)}$	$2.456\,\kappa_Z^2 + 0.456\,\kappa_t^2 - 1.903\,\kappa_Z\kappa_t$ $- 0.011\,\kappa_Z\kappa_b + 0.003\,\kappa_t\kappa_b$
$\sigma(WH)$	-	-	-	κ_W^2
$\sigma(t\bar{t}H)$	-	-	-	κ_t^2
$\sigma(tHW)$	-	t–W	-	$2.909\,\kappa_t^2 + 2.310\,\kappa_W^2 - 4.220\,\kappa_t\kappa_W$
$\sigma(tHq)$	-	t–W	-	$2.633\,\kappa_t^2 + 3.578\,\kappa_W^2 - 5.211\,\kappa_t\kappa_W$
$\sigma(b\bar{b}H)$	-	-	-	κ_b^2
Partial decay width				
Γ^{bb}	-	-	-	κ_b^2
Γ^{WW}	-	-	-	κ_W^2
Γ^{gg}	✓	t–b	κ_g^2	$1.111\,\kappa_t^2 + 0.012\,\kappa_b^2 - 0.123\,\kappa_t\kappa_b$
$\Gamma^{\tau\tau}$	-	-	-	κ_τ^2
Γ^{ZZ}	-	-	-	κ_Z^2
Γ^{cc}	-	-	-	$\kappa_c^2\ (=\kappa_t^2)$
$\Gamma^{\gamma\gamma}$	✓	t–W	κ_γ^2	$1.589\,\kappa_W^2 + 0.072\,\kappa_t^2 - 0.674\,\kappa_W\kappa_t$ $+0.009\,\kappa_W\kappa_\tau + 0.008\,\kappa_W\kappa_b$ $-0.002\,\kappa_t\kappa_b - 0.002\,\kappa_t\kappa_\tau$
$\Gamma^{Z\gamma}$	✓	t–W	$\kappa_{(Z\gamma)}^2$	$1.118\,\kappa_W^2 - 0.125\,\kappa_W\kappa_t + 0.004\,\kappa_t^2 + 0.003\,\kappa_W\kappa_b$
Γ^{ss}	-	-	-	$\kappa_s^2\ (=\kappa_b^2)$
$\Gamma^{\mu\mu}$	-	-	-	κ_μ^2
Total width $(B_{\text{i.}} = B_{\text{u.}} = 0)$				
Γ_H	✓	-	κ_H^2	$0.581\,\kappa_b^2 + 0.215\,\kappa_W^2 + 0.082\,\kappa_g^2$ $+0.063\,\kappa_\tau^2 + 0.026\,\kappa_Z^2 + 0.029\,\kappa_c^2$ $+0.0023\,\kappa_\gamma^2 + 0.0015\,\kappa_{(Z\gamma)}^2$ $+0.0004\,\kappa_s^2 + 0.00022\,\kappa_\mu^2$

7.2 Fermion and gauge boson couplings

The model studied in this section probes the universal coupling-strength scale factors $\kappa_V = \kappa_W = \kappa_Z$ for all vector bosons and $\kappa_F = \kappa_t = \kappa_b = \kappa_\tau = \kappa_\mu$ for all fermions. The effective couplings corresponding to the ggH and $H \to \gamma\gamma$ vertex loops are resolved in terms of the fundamental SM couplings. It is assumed that there are no invisible or undetected Higgs boson decays, i.e. $B_i. = B_u. = 0$. Only the relative sign between κ_V and κ_F is physical. As a negative relative sign has been excluded with high confidence level [9], $\kappa_V \geq 0$ and $\kappa_F \geq 0$ are assumed. The best-fit values and uncertainties from a combined fit are

$$\kappa_V = 1.03 \pm 0.03$$
$$\kappa_F = 0.97 \pm 0.07.$$

Figure 11 shows the results of the combined fit in the (κ_V, κ_F) plane. Both κ_V and κ_F are measured to be compatible with the SM expectation. The level of compatibility between the SM hypothesis with the best-fit point corresponds to a p-value of $p_{SM} = 45\%$, computed using the procedure outlined in Section 4 with two degrees of freedom. In the combined measurement a linear correlation of 50% between κ_V and κ_F is observed.
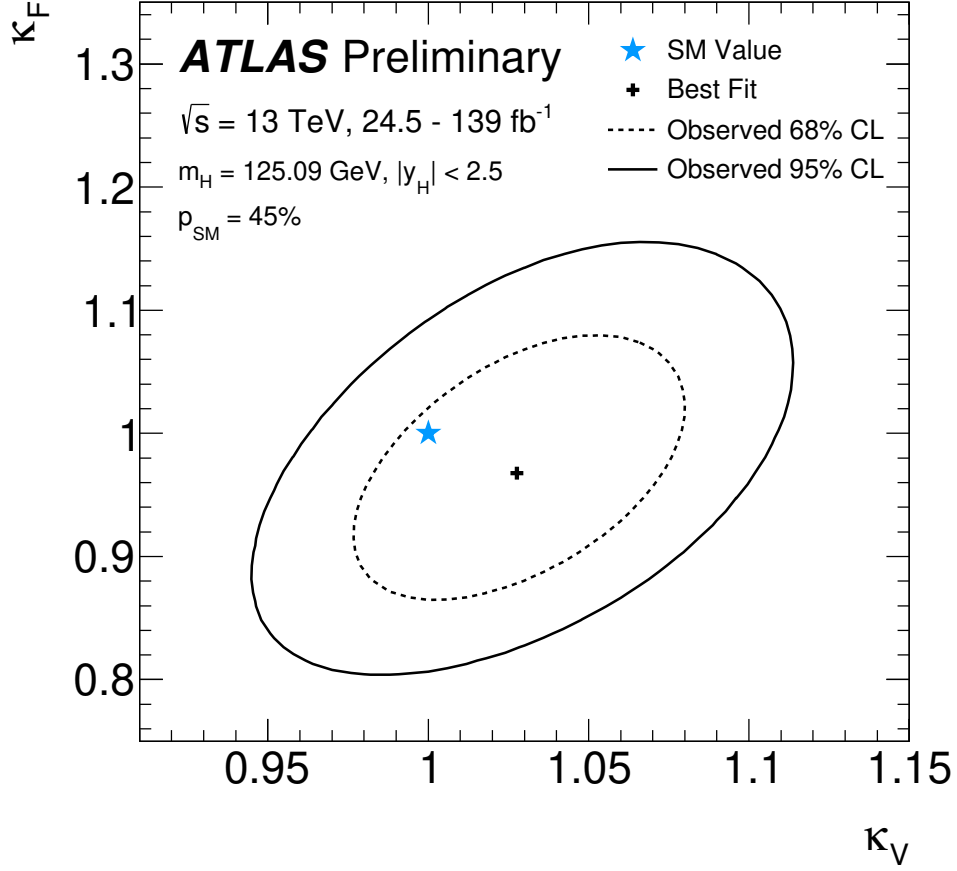
Figure 11: Negative log-likelihood contours at 68% and 95% CL in the (κ_V, κ_F) plane obtained from a combined fit, assuming no contributions from invisible or undetected Higgs boson decays. The best-fit value is indicated by a cross while the SM hypothesis is indicated by a star. A linear correlation of 50% between κ_V, κ_F is observed. The level of compatibility between the combined measurement and the SM prediction, estimated using the procedure outlined in the text with two degrees of freedom, corresponds to a p-value of $p_{SM} = 45\%$.

7.3 Probing BSM contributions in loops and decays

To probe contributions of new particles though loops, the effective coupling strengths to photons and gluons κ_γ and κ_g are measured. These parameters are defined to be positive as there is by construction no sensitivity to the sign of these coupling strengths. The modifiers corresponding to other loop-induced processes are resolved. Any potential BSM contribution to κ_γ and κ_g, corresponding to a deviation from one, may also contribute to the total width of the Higgs boson. To check this, the branching fractions $B_{i.}$ and $B_{u.}$, defined in Section 7.1, can be fixed to zero or allowed free in the fit. Furthermore, the benchmark models studied in this section assume that all coupling-strength modifiers of known SM particles are unity, i.e. they follow the SM predictions, and that the kinematics of the Higgs boson decay products are not altered significantly.

Assuming $B_{i.} = B_{u.} = 0$, the best-fit values and uncertainties from a combined fit are

$$\kappa_\gamma = 1.06 \pm 0.05$$
$$\kappa_g = 0.98 \pm 0.05.$$

Figure 12 shows negative log-likelihood contours obtained from the combined fit in the $(\kappa_\gamma, \kappa_g)$ plane. Both κ_γ and κ_g are measured to be compatible with the SM expectation. The level of compatibility between the SM hypothesis with the best-fit point corresponds to a p-value of $p_{SM} = 51\%$, computed using the procedure outlined in Section 4 with two degrees of freedom. A linear correlation of -34% between κ_γ and κ_g is observed, in part due to the constraint on their product from the rate of $H \to \gamma\gamma$ decays in the ggF channel.

To also consider additional contributions to the total width of the Higgs boson, the assumption of no invisible or undetected decays is dropped and B_i and B_u are included as independent parameters in the model. The measurement sensitive to Higgs boson decays into invisible final states described in Section 3.5 is included in the combination and used to constrain B_i. The B_u parameter is constrained by decay modes that do not involve a loop process. The results from this model are

$$\kappa_\gamma = 1.04^{+0.06}_{-0.05}$$
$$\kappa_g = 0.94^{+0.07}_{-0.06}$$
$$B_i = 0.00 \pm 0.07$$
$$B_u = -0.09^{+0.12}_{-0.13}.$$

Limits on B_i and B_u are set using the $\tilde{t}_\mu$ prescription presented in Section 4. The observed (expected) upper limits at 95% CL on B_i and B_u are 0.13 (0.13) and 0.16 (0.23), respectively. The level of compatibility between the SM hypothesis with the best-fit point corresponds to a p-value of $p_{SM} = 70\%$, computed using the procedure outlined in Section 4 with four degrees of freedom.
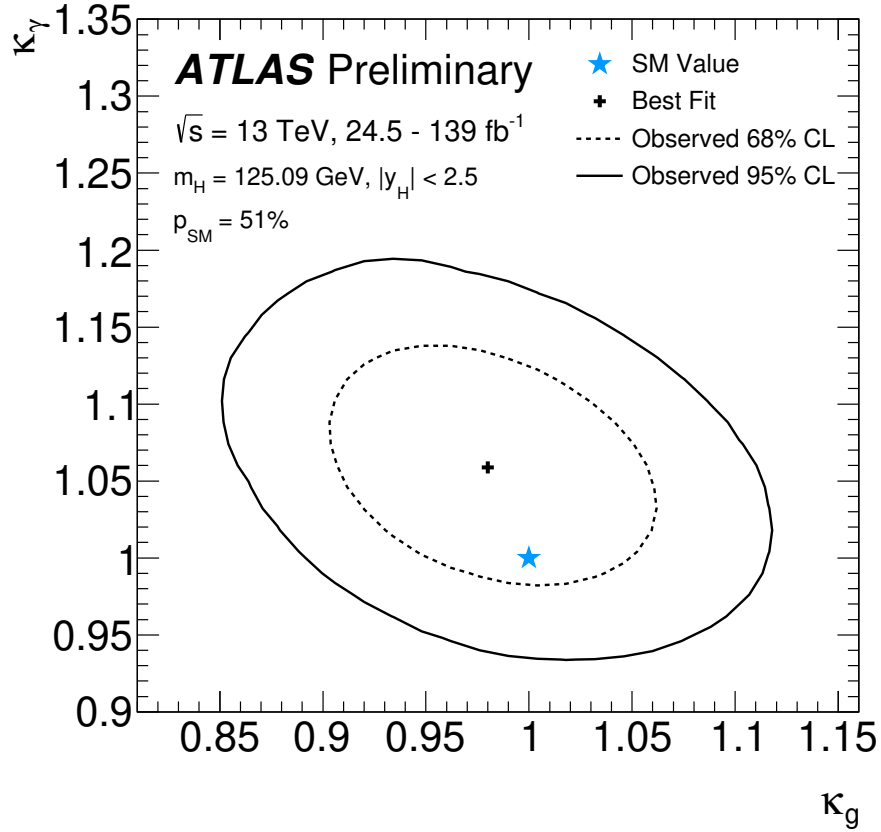
The results for both models are summarized in Figure 13.

Figure 12: Negative log-likelihood contours at 68% and 95% CL in the (κ_γ, κ_g) plane obtained from a combined fit, constraining all other coupling-strength modifiers to their SM values and assuming no contributions from invisible or undetected Higgs boson decays. The best-fit value for each measurement is indicated by a cross while the SM hypothesis is indicated by a star. A linear correlation of -34% between κ_γ and κ_g is observed. The level of compatibility between the combined measurement and the SM prediction, estimated using the procedure outlined in the text with two degrees of freedom, corresponds to a p-value of $p_{SM} = 51\%$.
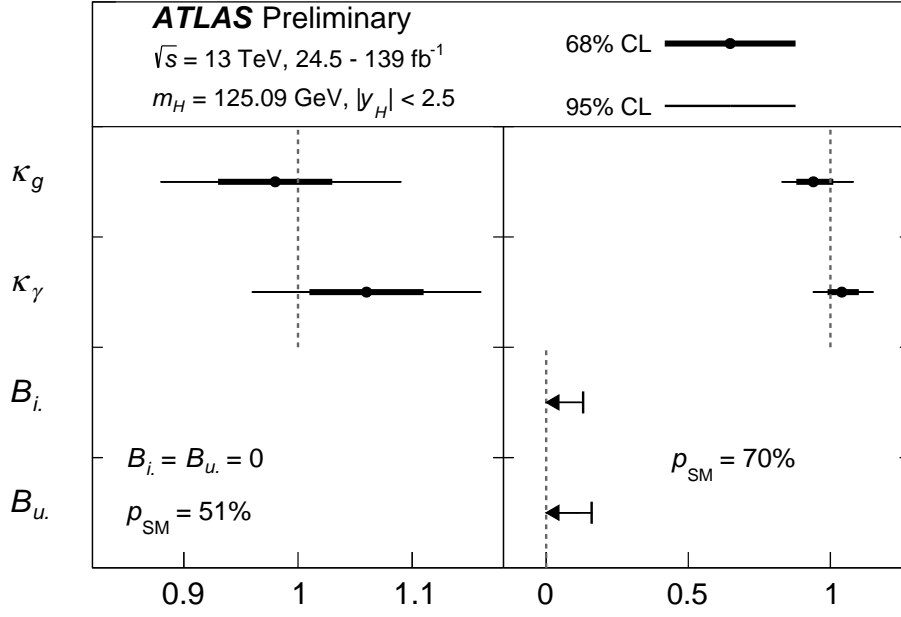
Figure 13: Best-fit values and uncertainties for effective modifiers to the photon and gluon couplings of the Higgs boson, with either $B_{\mathrm{i.}} = B_{\mathrm{u.}} = 0$ (left), or $B_{\mathrm{i.}}$ and $B_{\mathrm{u.}}$ included as free parameters (right). In the latter case, the measurement of the Higgs boson decay rate into invisible final states is included in the combination. The SM corresponds to $\kappa_\gamma = \kappa_g = 1$ and $B_{\mathrm{i.}} = B_{\mathrm{u.}} = 0$. All coupling-strength modifiers of known SM particles are assumed to be unity, i.e. they follow the SM predictions. The level of compatibility between the combined measurement and the SM prediction, estimated using the procedure outlined in the text with two (four) degrees of freedom for left (right), corresponds to a p-value of $p_{\mathrm{SM}} = 51\%$ (70%).

7.4 Generic parameterization assuming no new particles in loops and decays

In this model the scale factors for the coupling strengths to W, Z, t, b, τ and μ are treated independently. The Higgs boson couplings to second-generation quarks are assumed to scale as the couplings to the third-generation quarks. SM values are assumed for the couplings to first-generation fermions. Furthermore, it is assumed that only SM particles contribute to Higgs boson vertices involving loops, and modifications of the coupling-strength scale factors for fermions and vector bosons are propagated through the loop calculations. Invisible or undetected Higgs boson decays are assumed not to exist. All coupling-strength scale factors are assumed to be positive. The results of the $H \to \mu\mu$ analysis are included for this specific benchmark model. The results are shown in Table 7. The observed (expected) significance on κ_μ relative to the absence of this coupling is $2.1\,\sigma$ ($1.7\,\sigma$). The observed significance is slightly higher compared with the one reported in Ref. [19] both due to other coupling strengths being profiled to the combined dataset instead of fixed to SM, and to the pulling of nuisance parameters correlated with other channels. All measured coupling-strength scale factors in this generic model are found to be compatible with their SM expectation. The level of compatibility between the SM hypothesis with the best-fit point corresponds to a p-value of $p_{\mathrm{SM}} = 84\%$, computed using the procedure outlined in Section 4 with six degrees of freedom. Figure 14 shows the results of this benchmark model in terms of reduced coupling-strength scale factors, defined as

$$y_V = \sqrt{\kappa_V \frac{g_V}{2v}} = \sqrt{\kappa_V} \frac{m_V}{v}$$

for weak bosons with a mass m_V, where g_V is the absolute Higgs boson coupling strength and $v = 246\,\mathrm{GeV}$ is the vacuum expectation value of the Higgs field, and

$$y_F = \kappa_F \frac{g_F}{\sqrt{2}} = \kappa_F \frac{m_F}{v}$$

for fermions with a mass m_F. For the b quark and the top quark, the $\overline{MS}$ running mass evaluated at a scale of $125.09\,\mathrm{GeV}$ is used.

Table 7: Fit results for κ_Z, κ_W, κ_b, κ_t, κ_τ and κ_μ, all assumed to be positive. In this benchmark model BSM contributions to Higgs boson decays are assumed not to exist and Higgs boson vertices involving loops are resolved in terms of their SM content.

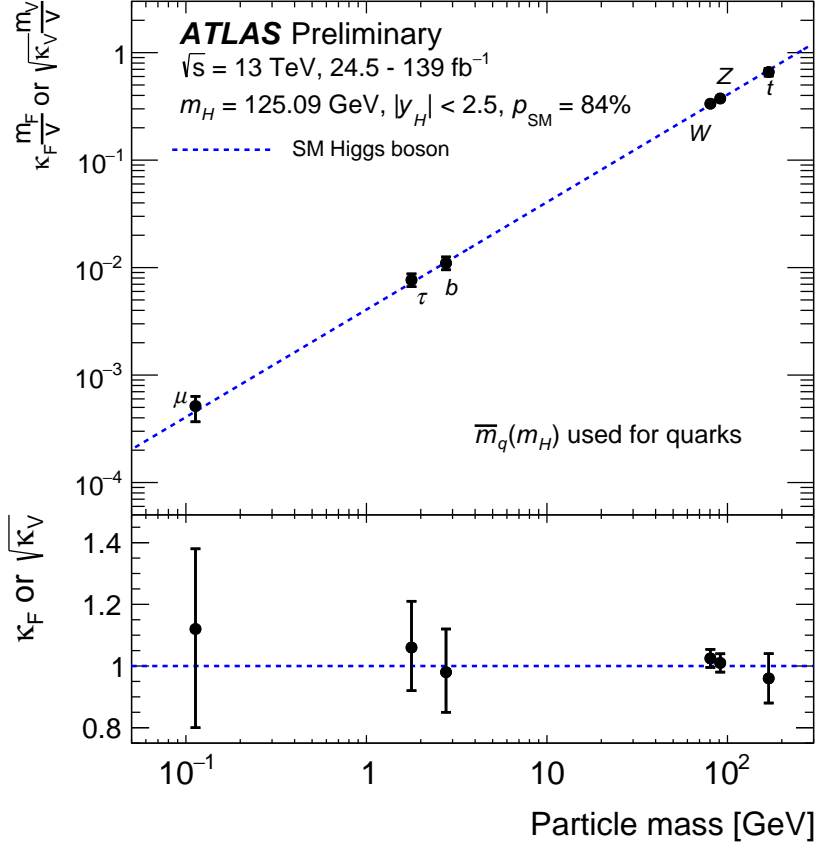| Parameter	Result
κ_Z	1.02 ± 0.06
κ_W	1.05 ± 0.06
κ_b	$0.98\,^{+\,0.14}_{-\,0.13}$
κ_t	$0.96\ \pm 0.08$
κ_τ	$1.06\,^{+\,0.15}_{-\,0.14}$
κ_μ	$1.12\,^{+\,0.26}_{-\,0.32}$

Figure 14: Reduced coupling-strength modifiers $\kappa_F \frac{m_F}{v}$ for fermions ($F = t, b, \tau, \mu$) and $\sqrt{\kappa_V} \frac{m_V}{v}$ for weak gauge bosons ($V = W, Z$) as a function of their masses m_F and m_V, respectively, and the vacuum expectation value of the Higgs field $v = 246$ GeV. The SM prediction for both cases is also shown (dotted line). The black error bars represent 68% CL intervals for the measured parameters. The coupling modifiers are measured assuming no BSM contributions to the Higgs boson decays, and the SM structure of loop processes such as ggF and $H \rightarrow \gamma\gamma$. The lower inset shows the ratios of the values to their SM predictions. The level of compatibility between the combined measurement and the SM prediction, estimated using the procedure outlined in the text with six degrees of freedom, corresponds to a p-value of $p_{\mathrm{SM}} = 84\%$.

7.5 Generic parameterization including effective photon and gluon couplings with and without BSM contributions in decays

The models considered in this section are based on the same parameterization as the one in Section 7.4 but the ggF, $H \rightarrow gg$, and $H \rightarrow \gamma\gamma$ loop processes are parameterized using the effective coupling-strength modifiers κ_g and κ_γ, similar to the benchmark model probed in Section 7.3.

The measured parameters include κ_Z, κ_W, κ_b, κ_t, κ_τ, κ_γ and κ_g. The sign of κ_t can be either positive or negative, while κ_Z is assumed to be positive without loss of generality. All other model parameters are also assumed to be positive. Furthermore it is assumed that any potential BSM effect does not affect the kinematics of the Higgs boson decay products significantly. Two alternative scenarios are considered for

the total width of the Higgs boson:

(a) No BSM contributions to the total width ($B_i = B_u = 0$).

(b) Both B_i and B_u are added as free parameters to the model. The measurement of Higgs boson decays into invisible final states, VBF, $H \rightarrow inv$, described in Section 3.5 is included in the combination, for these results only, and used to provide a constraint on B_i. The conditions $\kappa_W \leq 1$ and $\kappa_Z \leq 1$ are used to provide a constraint on B_u as discussed in Section 7.1.

The numerical results for the two scenarios are summarized in Table 8 and illustrated in Figure 15. Limits on B_i and B_u are set using the $\tilde{t}_\mu$ prescription presented in Section 4. All probed fundamental coupling-strength scale factors, as well as the probed loop-induced coupling scale factors are measured to be compatible with their SM expectation for both explored assumptions. Upper limits are set on the fraction of Higgs boson decays into invisible or undetected decays. In scenario (a) with no BSM contribution to the total width, a possible negative value for κ_t is excluded at 2.9σ (2.7σ expected) with sensitivity coming from the tH and $gg \rightarrow ZH$ processes. In scenario (b) the observed (expected) 95% CL upper limits on the branching fractions are $B_i < 0.09$ (0.11) and $B_u < 0.19$ (0.25), and the lower limits on the couplings to vector bosons are $\kappa_Z > 0.88$ (0.86) and $\kappa_W > 0.89$ (0.84). The level of compatibility between the SM hypothesis with the best-fit point in scenario (a) corresponds to a p-value of $p_{SM} = 92\%$, computed using the procedure outlined in Section 4 with seven degrees of freedom.

Table 8: Fit results for Higgs boson coupling modifiers per particle type with effective photon and gluon couplings and either (a) $B_i = B_u = 0$, or (b) B_i and B_u included as free parameters, with the conditions $\kappa_{W,Z} \leq 1$ applied and the measurement of the Higgs boson decay rate into invisible final states included in the combination. The SM corresponds to $B_i = B_u = 0$ and all κ parameters set to unity. All κ parameters except for κ_t are assumed to be positive.

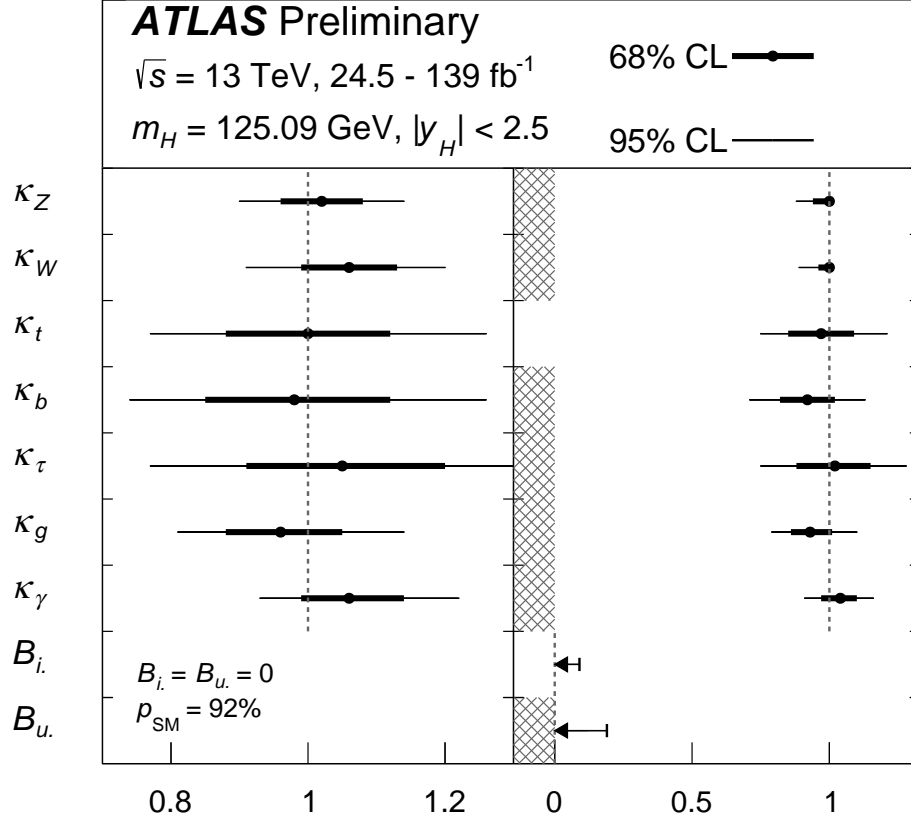| Parameter	(a) $B_i = B_u = 0$	(b) B_i free, $B_u \geq 0$, $\kappa_{W,Z} \leq 1$
κ_Z	1.02 ± 0.06	> 0.88 at 95% CL
κ_W	1.06 ± 0.07	> 0.89 at 95% CL
κ_b	$0.98 ^{+0.14}_{-0.13}$	0.92 ± 0.10
κ_t	1.00 ± 0.12	0.97 ± 0.12
κ_τ	$1.05 ^{+0.15}_{-0.14}$	$1.02 ^{+0.13}_{-0.14}$
κ_γ	$1.06 ^{+0.08}_{-0.07}$	$1.04 ^{+0.06}_{-0.07}$
κ_g	$0.96 ^{+0.09}_{-0.08}$	$0.93 ^{+0.08}_{-0.07}$
B_i	-	< 0.09 at 95% CL
B_u	-	< 0.19 at 95% CL

Figure 15: Best-fit values and uncertainties for Higgs boson coupling modifiers per particle type with effective photon and gluon couplings and either $B_{i.} = B_{u.} = 0$ (left), or $B_{i.}$ and $B_{u.}$ included as free parameters with the conditions $\kappa_{W,Z} \leq 1$ applied and the measurement of the Higgs boson decay rate into invisible final states included in the combination (right). The SM corresponds to $B_{i.} = B_{u.} = 0$ and all κ parameters set to unity. All parameters except κ_t are assumed to be positive. In the former case, the level of compatibility between the combined measurement and the SM prediction, estimated using the procedure outlined in the text with seven degrees of freedom, corresponds to a p-value of $p_{SM} = 92\%$.

7.6 Generic parameterization using ratios of coupling modifiers

The five absolute coupling-strength scale factors and two effective loop-coupling scale factors measured in the previous benchmark model are expressed as ratios of scale factors that can be measured independent of any assumptions about the Higgs boson total width, together with a global scale factor determined by the $gg \rightarrow H \rightarrow ZZ^*$ process. The model parameters are defined in Table 9. All parameters are assumed to be positive. This parameterization represents the most model-independent determination of coupling-strength scale factors that is currently possible in the κ-framework. The numerical results from the fit to this benchmark model are summarized in Table 9 and visualized in Figure 16. All model parameters are measured to be compatible with their SM expectation. The level of compatibility between the SM hypothesis with the best-fit point corresponds to a p-value of $p_{\mathrm{SM}} = 92\%$, computed using the procedure outlined in Section 4 with seven degrees of freedom.

The parameter λ_{WZ} in this model is of particular interest: identical coupling-strength scale factors for the W and Z bosons are required within tight bounds by the SU(2) custodial symmetry and the ρ parameter measurements at LEP and at the Tevatron [131]. The ratio $\lambda_{\gamma Z}$ is sensitive to new charged particles contributing to the $H \rightarrow \gamma\gamma$ loop unlike in $H \rightarrow ZZ^*$ decays. Similarly, the ratio λ_{tg} is sensitive to new colored particles contributing through the ggF loop unlike in $t\bar{t}H$ or tH events. The observed values are in agreement with the SM expectation.

Table 9: Best-fit values and uncertainties for ratios of coupling modifiers. The second column provides the expression of the measured parameters in terms of the coupling modifiers defined in previous sections. All parameters are defined to be unity in the SM.

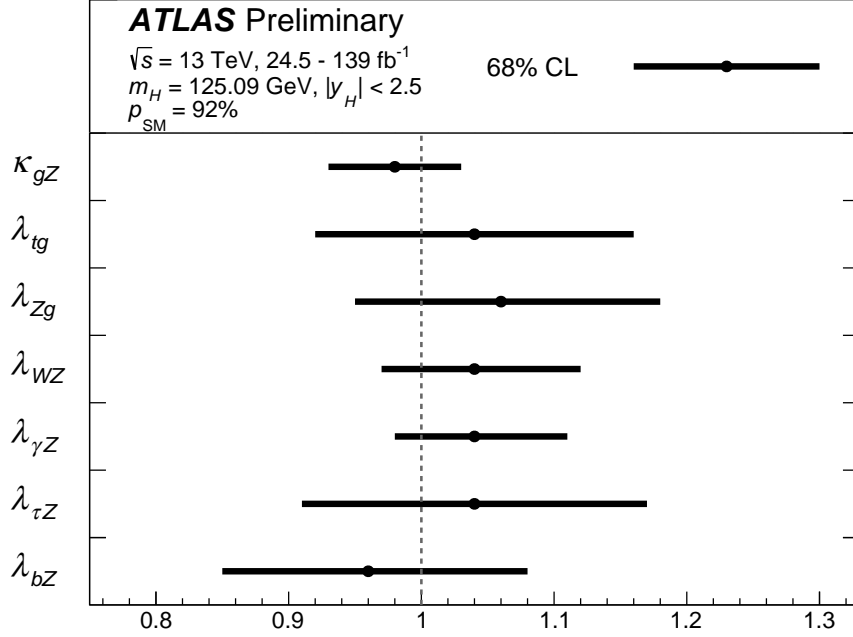| Parameter	Definition in terms of κ modifiers	Result
κ_{gZ}	$\kappa_g \kappa_Z / \kappa_H$	0.98 ± 0.05
λ_{tg}	κ_t / κ_g	1.04 ± 0.12
λ_{Zg}	κ_Z / κ_g	$1.06\,^{+\,0.12}_{-\,0.11}$
λ_{WZ}	κ_W / κ_Z	$1.04\,^{+\,0.08}_{-\,0.07}$
$\lambda_{\gamma Z}$	κ_γ / κ_Z	$1.04\,^{+\,0.07}_{-\,0.06}$
$\lambda_{\tau Z}$	κ_τ / κ_Z	1.04 ± 0.13
λ_{bZ}	κ_b / κ_Z	$0.96\,^{+\,0.12}_{-\,0.11}$

Figure 16: Measured ratios of coupling modifiers. The dashed line indicates the SM value of unity for each parameter. The level of compatibility between the combined measurement and the SM prediction, estimated using the procedure outlined in the text with seven degrees of freedom, corresponds to a p-value of $p_{\mathrm{SM}} = 92\%$.

8 Constraints on new phenomena

Two-Higgs-doublet models (2HDMs) [43, 132–134] are a promising extension of the SM. The measurements are interpreted in terms of this benchmark model, providing indirect limits on its parameters. The interpretations presented in this section follow the procedure discussed in Ref. [44].

In 2HDMs, the SM Higgs sector is extended by introducing an additional complex isodoublet scalar field with weak hypercharge one. Four types of 2HDMs satisfy the Paschos–Glashow–Weinberg condition [135, 136], which prevents the appearance of tree-level flavor-changing neutral currents:

- Type I: One Higgs doublet couples to vector bosons, while the other one couples to fermions. The first doublet is *fermiophobic* in the limit where the two Higgs doublets do not mix.

- Type II: One Higgs doublet couples to up-type quarks and the other one to down-type quarks and charged leptons.

- Lepton-specific: The Higgs bosons have the same couplings to quarks as in the Type I model and to charged leptons as in Type II.

- Flipped: The Higgs bosons have the same couplings to quarks as in the Type II model and to charged leptons as in Type I.

The observed Higgs boson is identified with the light CP-even neutral scalar h predicted by 2HDMs, and its accessible production and decay modes are assumed to be the same as those of the SM Higgs

boson. Furthermore, it is assumed that only the 2HDMs are responsible for the potential BSM effects in the Higgs boson couplings to vector bosons, up-type quarks, down-type quarks and leptons. The changes with respect to the corresponding SM predictions are expressed as functions of the mixing angle α between h and the heavy CP-even neutral scalar, and the ratio of the vacuum expectation values of the Higgs doublets, $\tan\beta$ [44].

Figure 17 shows the regions of the $(\cos(\beta - \alpha), \tan\beta)$ plane that are excluded at a confidence level of 95 % or higher, for each of the four types of 2HDMs. The expected exclusion limits in the SM hypothesis are also overlaid. The data are consistent with the alignment limit [134] at $\cos(\beta - \alpha) = 0$, in which the couplings of h match those of the SM Higgs boson, within one standard deviation or better in each of the tested models. The allowed regions also include narrow, curved *petal* regions at positive $\cos(\beta - \alpha)$ and moderate $\tan\beta$ in the Type II, Lepton-specific, and Flipped models. These correspond to regions with $\cos(\beta + \alpha) \approx 0$, for which some fermion couplings have the same magnitude as in the SM, but the opposite sign.
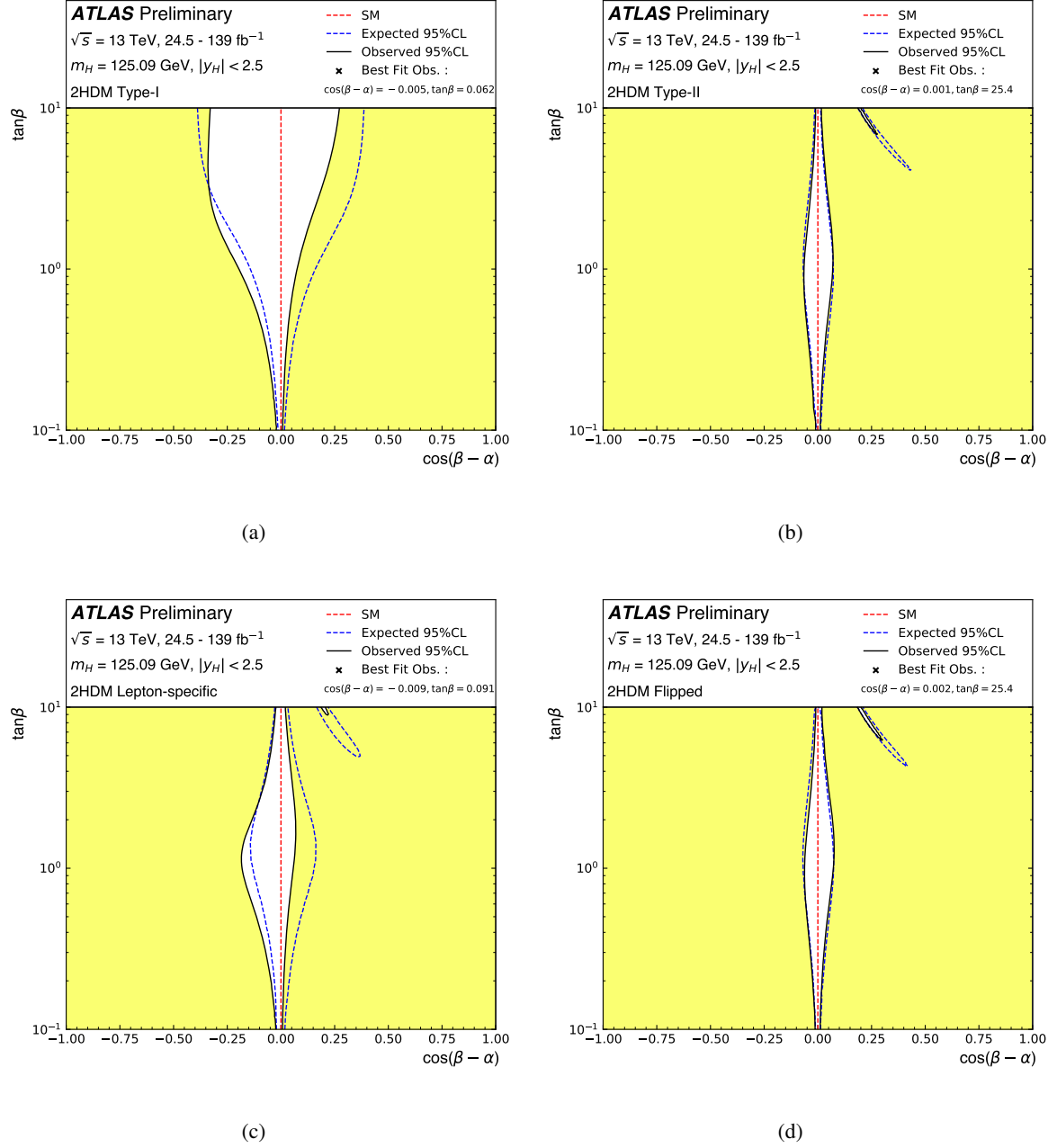
Figure 17: Regions of the $(\cos(\beta - \alpha), \tan\beta)$ plane of four types of 2HDMs excluded by fits to the measured rates of Higgs boson production and decays. Contours at 95% CL, defined in the asymptotic approximation by $-2\ln\Lambda = 5.99$, are drawn for both the data and the expectation for the SM Higgs sector. In all cases, the observed best-fit points are out of the range, and are thus provided as numerical values instead. The angles α and β are taken to satisfy $0 \le \beta \le \pi/2$ and $0 \le \beta - \alpha \le \pi$ without loss of generality. The alignment limit at $\cos(\beta - \alpha) = 0$, in which all Higgs boson couplings take their SM values, is indicated by the dashed red line.

9 Conclusions

Measurements of Higgs boson production cross sections and branching fractions have been performed using up to 139 fb^{-1} of pp collision data produced by the LHC at $\sqrt{s}$ = 13 TeV and recorded by the ATLAS detector. The results presented in this note are based on the combination of analyses of the $H \rightarrow \gamma\gamma$, $H \rightarrow ZZ^*$, $H \rightarrow WW^*$, $H \rightarrow \tau\tau$, $H \rightarrow b\bar{b}$, and $H \rightarrow \mu\mu$ decay modes and a search for decays into invisible final states in the VBF production mode.

The global signal strength is determined to be $\mu = 1.06 \pm 0.07$.

The Higgs boson production cross sections within the region $|y_H| < 2.5$ are measured in a combined fit for the gluon–gluon fusion process, vector-boson fusion, the associated production with a W or Z boson and the associated production with top quarks, assuming the SM Higgs boson branching fractions. The combined measurement leads to an observed significance above 5σ for the ggF, VBF, WH, ZH and $t\bar{t}H + tH$ production processes. The observed (expected) significance for the WH and ZH modes are respectively $6.3\,\sigma$ ($5.2\,\sigma$) and $5.0\,\sigma$ ($5.4\,\sigma$), corresponding to a first observation for WH. Several other measurements have been performed, including production cross section times branching fraction for each pair of production and decay processes, and ratios of production cross sections relative to ggF and ratios of branching fractions relative to $H \rightarrow ZZ^*$, together with the cross section of $gg \rightarrow H \rightarrow ZZ^*$ process. Measurements are also provided in the Simplified Template Cross-section framework. In addition, the measurements are interpreted in terms of the coupling strength modifiers (κ-framework), and as constraints on Two-Higgs-Doublet Models. In all cases, no significant deviations from SM predictions are observed.

References

[1] F. Englert and R. Brout, *Broken Symmetry and the Mass of Gauge Vector Mesons*, Phys. Rev. Lett. **13** (1964) 321 (cit. on p. 2).

[2] P. W. Higgs, *Broken symmetries, massless particles and gauge fields*, Phys. Lett. **12** (1964) 132 (cit. on p. 2).

[3] P. W. Higgs, *Broken Symmetries and the Masses of Gauge Bosons*, Phys. Rev. Lett. **13** (1964) 508 (cit. on p. 2).

[4] G. S. Guralnik, C. R. Hagen, and T. W. .B. Kibble, *Global conservation laws and massless particles*, Phys. Rev. Lett. **13** (1964) 585 (cit. on p. 2).

[5] P. W. Higgs, *Spontaneous symmetry breakdown without massless bosons*, Phys. Rev. **145** (1966) 1156 (cit. on p. 2).

[6] T. W. B. Kibble, *Symmetry breaking in non-Abelian gauge theories*, Phys. Rev. **155** (1967) 1554 (cit. on p. 2).

[7] ATLAS Collaboration, *Observation of a new particle in the search for the Standard Model Higgs boson with the ATLAS detector at the LHC*, Phys. Lett. B **716** (2012) 1, arXiv: 1207.7214 [hep-ex] (cit. on p. 2).

[8] CMS Collaboration, *Observation of a new boson at a mass of 125 GeV with the CMS experiment at the LHC*, Phys. Lett. B **716** (2012) 30, arXiv: 1207.7235 [hep-ex] (cit. on p. 2).

[9] ATLAS and CMS Collaborations, *Measurements of the Higgs boson production and decay rates and constraints on its couplings from a combined ATLAS and CMS analysis of the LHC pp collision data at $\sqrt{s}$ = 7 and 8 TeV*, JHEP **08** (2016) 045, arXiv: 1606.02266 [hep-ex] (cit. on pp. 2, 8, 10, 30).

[10] ATLAS Collaboration, *Measurement of the properties of Higgs boson production at $\sqrt{s}$ = 13 TeV in the H → γγ channel using 139 fb^{-1} of pp collision data with the ATLAS experiment*, ATLAS-CONF-2020-026, 2020, URL: https://atlas.web.cern.ch/Atlas/GROUPS/PHYSICS/CONFNOTES/ATLAS-CONF-2020-026 (cit. on pp. 2, 3, 5, 7, 21).

[11] ATLAS Collaboration, *Higgs boson production cross-section measurements and their EFT interpretation in the 4ℓ decay channel at $\sqrt{s}$ = 13 TeV with the ATLAS detector*, Submitted to: EPJC (2020), arXiv: 2004.03447 [hep-ex] (cit. on pp. 2, 3, 6, 21).

[12] ATLAS Collaboration, *Measurements of gluon-gluon fusion and vector-boson fusion Higgs boson production cross-sections in the H → WW* → eνμν decay channel in pp collisions at $\sqrt{s}$ = 13 TeV with the ATLAS detector*, Phys. Lett. B **789** (2019) 508, arXiv: 1808.09054 [hep-ex] (cit. on pp. 2, 3).

[13] ATLAS Collaboration, *Cross-section measurements of the Higgs boson decaying into a pair of τ-leptons in proton–proton collisions at $\sqrt{s}$ = 13 TeV with the ATLAS detector*, Phys. Rev. D **99** (2019) 072001, arXiv: 1811.08856 [hep-ex] (cit. on pp. 2, 3).

[14] ATLAS Collaboration, *Measurements of WH and ZH production in the H → bb decay channel in pp collisions at 13 TeV with the ATLAS detector*, Submitted to EPJC (2020), arXiv: 2007.02873 [hep-ex] (cit. on pp. 2, 3, 6).

[15] ATLAS Collaboration, *Search for Higgs bosons produced via vector-boson fusion and decaying into bottom quark pairs in $\sqrt{s}$ = 13 TeV pp collisions with the ATLAS detector*, Phys. Rev. D **98** (2018) 052003, arXiv: 1807.08639 [hep-ex] (cit. on pp. 2, 3).

[16] ATLAS Collaboration, *Evidence for the associated production of the Higgs boson and a top quark pair with the ATLAS detector*, Phys. Rev. D **97** (2018) 072003, arXiv: 1712.08891 [hep-ex] (cit. on pp. 2–4).

[17] ATLAS Collaboration, *Search for the standard model Higgs boson produced in association with top quarks and decaying into a b$\bar{b}$ pair in pp collisions at $\sqrt{s}$ = 13 TeV with the ATLAS detector*, Phys. Rev. D **97** (2018) 072016, arXiv: 1712.08895 [hep-ex] (cit. on pp. 2–4).

[18] ATLAS Collaboration, *Observation of Higgs boson production in association with a top quark pair at the LHC with the ATLAS detector*, Phys. Lett. B **784** (2018) 173, arXiv: 1806.00425 [hep-ex] (cit. on pp. 2, 3).

[19] ATLAS Collaboration, *Search for the dimuon decay of the Standard Model Higgs Boson with the ATLAS Detector*, Submitted to Phys. Lett. B (2020), arXiv: 2007.07830 [hep-ex] (cit. on pp. 2, 3, 7, 35).

[20] ATLAS Collaboration, *Search for invisible Higgs boson decays with vector boson fusion signatures with the ATLAS detector using an integrated luminosity of 139 fb^{-1}*, ATLAS-CONF-2020-008, 2020, URL: https://atlas.web.cern.ch/Atlas/GROUPS/PHYSICS/CONFNOTES/ATLAS-CONF-2020-008 (cit. on pp. 2, 3, 7).

[21] ATLAS Collaboration, *Combined measurements of Higgs boson production and decay using up to 80 fb^{-1} of proton–proton collision data at $\sqrt{s}$ = 13 TeV collected with the ATLAS experiment*, Phys. Rev. D **101** (2020) 012002, arXiv: 1909.02845 [hep-ex] (cit. on pp. 2, 5–7, 13, 28).

[22] ATLAS Collaboration, *Search for invisible Higgs boson decays in vector boson fusion at $\sqrt{s}$ = 13 TeV with the ATLAS detector*, Phys. Lett. B **793** (2019) 499, arXiv: 1809.06682 [hep-ex] (cit. on p. 2).

[23] ATLAS Collaboration, *Search for an invisibly decaying Higgs boson or dark matter candidates produced in association with a Z boson in pp collisions at $\sqrt{s}$ = 13 TeV with the ATLAS detector*, Phys. Lett. B **776** (2018) 318, arXiv: 1708.09624 [hep-ex] (cit. on p. 2).

[24] ATLAS Collaboration, *Search for dark matter in events with a hadronically decaying vector boson and missing transverse momentum in pp collisions at $\sqrt{s}$ = 13 TeV with the ATLAS detector*, JHEP **10** (2018) 180, arXiv: 1807.11471 [hep-ex] (cit. on p. 2).

[25] ATLAS Collaboration, *Combination of Searches for Invisible Higgs Boson Decays with the ATLAS Experiment*, Phys. Rev. Lett. **122** (2019) 231801, arXiv: 1904.05105 [hep-ex] (cit. on p. 2).

[26] ATLAS and CMS Collaborations, *Combined Measurement of the Higgs Boson Mass in pp Collisions at $\sqrt{s}$ = 7 and 8 TeV with the ATLAS and CMS Experiments*, Phys. Rev. Lett. **114** (2015) 191803, arXiv: 1503.07589 [hep-ex] (cit. on p. 2).

[27] CMS Collaboration, *Measurements of Higgs boson production via gluon fusion and vector boson fusion in the diphoton decay channel at $\sqrt{s}$ = 13 TeV*, CMS-PAS-HIG-18-029, 2019, URL: https://cds.cern.ch/record/2667225 (cit. on p. 2).

[28] CMS Collaboration, *Measurements of $t\bar{t}H$ production and the CP structure of the Yukawa interaction between the Higgs boson and top quark in the diphoton decay channel*, (2020), arXiv: 2003.10866 [hep-ex] (cit. on p. 2).

[29] CMS Collaboration, *Measurements of properties of the Higgs boson in the four-lepton final state in proton-proton collisions at $\sqrt{s}$ = 13 TeV*, CMS-PAS-HIG-19-001, 2019, URL: https://cds.cern.ch/record/2668684 (cit. on p. 2).

[30] CMS Collaboration, *Measurements of properties of the Higgs boson decaying to a W boson pair in pp collisions at $\sqrt{s}$ = 13 TeV*, Phys. Lett. B **791** (2019) 96, arXiv: 1806.05246 [hep-ex] (cit. on p. 2).

[31] CMS Collaboration, *Measurement of Higgs boson production and decay to the $\tau\tau$ final state*, CMS-PAS-HIG-18-032, 2019, URL: https://cds.cern.ch/record/2668685 (cit. on p. 2).

[32] CMS Collaboration, *Observation of Higgs Boson Decay to Bottom Quarks*, Phys. Rev. Lett. **121** (2018) 121801, arXiv: 1808.08242 [hep-ex] (cit. on p. 2).

[33] CMS Collaboration, *Measurement of $t\bar{t}H$ production in the H $\rightarrow$ b$\bar{b}$ decay channel in 41.5 fb^{-1} of proton-proton collision data at $\sqrt{s}$ = 13 TeV*, CMS-PAS-HIG-18-030, 2019, URL: https://cds.cern.ch/record/2675023 (cit. on p. 2).

[34] CMS Collaboration, *Evidence for associated production of a Higgs boson with a top quark pair in final states with electrons, muons, and hadronically decaying τ leptons at $\sqrt{s}$ = 13 TeV*, JHEP **08** (2018) 066, arXiv: 1803.05485 [hep-ex] (cit. on p. 2).

[35] CMS Collaboration, *Measurement of the associated production of a Higgs boson with a top quark pair in final states with electrons, muons and hadronically decaying τ leptons in data recorded in 2017 at $\sqrt{s}$ = 13 TeV*, CMS-PAS-HIG-18-019, 2018, URL: https://cds.cern.ch/record/2649199 (cit. on p. 2).

[36] CMS Collaboration, *Search for the Higgs Boson Decaying to Two Muons in Proton–Proton Collisions at $\sqrt{s}$ = 13 TeV*, Phys. Rev. Lett. **122** (2019) 021801, arXiv: 1807.06325 [hep-ex] (cit. on p. 2).

[37] CMS Collaboration, *Measurements of the Higgs boson width and anomalous HVV couplings from on-shell and off-shell production in the four-lepton final state*, Phys. Rev. D **99** (2019) 112003, arXiv: 1901.00174 [hep-ex] (cit. on p. 2).

[38] CMS Collaboration, *Combined Higgs boson production and decay measurements with up to 137 fb-1 of proton-proton collision data at $\sqrt{s}$ = 13 TeV*, CMS-PAS-HIG-19-005, 2020, URL: https://cds.cern.ch/record/2706103 (cit. on p. 2).

[39] LHC Higgs Cross Section Working Group, D. de Florian et al., *Handbook of LHC Higgs Cross Sections: 4. Deciphering the Nature of the Higgs Sector*, (2016), arXiv: 1610.07922 [hep-ph] (cit. on pp. 2, 4, 9, 11, 12, 15, 19, 20, 26, 29).

[40] J. R. Andersen et al., *Les Houches 2015: Physics at TeV Colliders Standard Model Working Group Report*, (2016), arXiv: 1605.04692 [hep-ph] (cit. on pp. 2, 20).

[41] N. Berger et al., *Simplified Template Cross Sections - Stage 1.1*, (2019), arXiv: 1906.02754 [hep-ph] (cit. on pp. 2, 20).

[42] S. Amoroso et al., "Les Houches 2019: Physics at TeV Colliders: Standard Model Working Group Report," *11th Les Houches Workshop on Physics at TeV Colliders: PhysTeV Les Houches*, 2020, arXiv: 2003.01700 [hep-ph] (cit. on pp. 2, 20).

[43] LHC Higgs Cross Section Working Group, S. Heinemeyer et al., *Handbook of LHC Higgs Cross Sections: 3. Higgs Properties*, CERN-2013-004 (2013), arXiv: 1307.1347 [hep-ph] (cit. on pp. 3, 27–29, 40).

[44] ATLAS Collaboration, *Constraints on new phenomena via Higgs boson couplings and invisible decays with the ATLAS detector*, JHEP **11** (2015) 206, arXiv: 1509.00672 [hep-ex] (cit. on pp. 3, 40, 41).

[45] ATLAS Collaboration, *The ATLAS Experiment at the CERN Large Hadron Collider*, JINST **3** (2008) S08003 (cit. on p. 3).

[46] ATLAS Collaboration, *ATLAS Insertable B-Layer Technical Design Report*, ATLAS-TDR-19, 2010, URL: https://cds.cern.ch/record/1291633 (cit. on p. 3), Addendum: ATLAS-TDR-19-ADD-1, 2012, URL: https://cds.cern.ch/record/1451888.

[47] B. Abbott et al., *Production and integration of the ATLAS Insertable B-Layer*, JINST **13** (2018) T05008, arXiv: 1803.00844 [physics.ins-det] (cit. on p. 3).

[48] ATLAS Collaboration, *Luminosity determination in pp collisions at $\sqrt{s}$ = 13 TeV using the ATLAS detector at the LHC*, ATLAS-CONF-2019-021, 2019, URL: https://cds.cern.ch/record/2677054 (cit. on p. 3).

[49] G. Avoni et al., *The new LUCID-2 detector for luminosity measurement and monitoring in ATLAS*, JINST **13** (2018) P07017 (cit. on p. 3).

[50] P. Nason, *A new method for combining NLO QCD with shower Monte Carlo algorithms*, JHEP **11** (2004) 040, arXiv: hep-ph/0409146 (cit. on p. 4).

[51] S. Frixione, P. Nason, and C. Oleari, *Matching NLO QCD computations with parton shower simulations: the POWHEG method*, JHEP **11** (2007) 070, arXiv: 0709.2092 [hep-ph] (cit. on p. 4).

[52] S. Alioli, P. Nason, C. Oleari, and E. Re, *A general framework for implementing NLO calculations in shower Monte Carlo programs: the POWHEG BOX*, JHEP **06** (2010) 043, arXiv: 1002.2581 [hep-ph] (cit. on p. 4).

[53] S. Alioli, P. Nason, C. Oleari, and E. Re, *NLO Higgs boson production via gluon fusion matched with shower in POWHEG*, JHEP **04** (2009) 002, arXiv: `0812.0578 [hep-ph]` (cit. on p. 4).

[54] K. Hamilton, P. Nason, E. Re, and G. Zanderighi, *NNLOPS simulation of Higgs boson production*, JHEP **10** (2013) 222, arXiv: `1309.0017 [hep-ph]` (cit. on p. 4).

[55] K. Hamilton, P. Nason, and G. Zanderighi, *Finite quark-mass effects in the NNLOPS POWHEG+MiNLO Higgs generator*, JHEP **05** (2015) 140, arXiv: `1501.04637 [hep-ph]` (cit. on p. 4).

[56] S. Catani and M. Grazzini, *Next-to-Next-to-Leading-Order Subtraction Formalism in Hadron Collisions and its Application to Higgs-Boson Production at the Large Hadron Collider*, Phys. Rev. Lett. **98** (2007) 222002, arXiv: `hep-ph/0703012` (cit. on p. 4).

[57] K. Hamilton, P. Nason, and G. Zanderighi, *MINLO: multi-scale improved NLO*, JHEP **10** (2012) 155, arXiv: `1206.3572 [hep-ph]` (cit. on p. 4).

[58] J. M. Campbell et al., *NLO Higgs Boson Production Plus One and Two Jets Using the POWHEG BOX, MadGraph4 and MCFM*, JHEP **07** (2012) 092, arXiv: `1202.5475 [hep-ph]` (cit. on p. 4).

[59] K. Hamilton, P. Nason, C. Oleari, and G. Zanderighi, *Merging H/W/Z + 0 and 1 jet at NLO with no merging scale: a path to parton shower + NNLO matching*, JHEP **05** (2013) 082, arXiv: `1212.4504 [hep-ph]` (cit. on p. 4).

[60] J. Butterworth et al., *PDF4LHC recommendations for LHC Run II*, J. Phys. G **43** (2016) 023001, arXiv: `1510.03865 [hep-ph]` (cit. on p. 4).

[61] C. Anastasiou, C. Duhr, F. Dulat, F. Herzog, and B. Mistlberger, *Higgs Boson Gluon-Fusion Production in QCD at Three Loops*, Phys. Rev. Lett. **114** (2015) 212001, arXiv: `1503.06056 [hep-ph]` (cit. on p. 4).

[62] C. Anastasiou et al., *High precision determination of the gluon fusion Higgs boson cross-section at the LHC*, JHEP **05** (2016) 058, arXiv: `1602.00695 [hep-ph]` (cit. on p. 4).

[63] F. Dulat, A. Lazopoulos, and B. Mistlberger, *iHixs 2 — Inclusive Higgs cross sections*, Comput. Phys. Commun. **233** (2018) 243, arXiv: `1802.00827 [hep-ph]` (cit. on p. 4).

[64] R. V. Harlander and K. J. Ozeren, *Finite top mass effects for hadronic Higgs production at next-to-next-to-leading order*, JHEP **11** (2009) 088, arXiv: `0909.3420 [hep-ph]` (cit. on p. 4).

[65] R. V. Harlander and K. J. Ozeren, *Top mass effects in Higgs production at next-to-next-to-leading order QCD: Virtual corrections*, Phys. Lett. **B679** (2009) 467, arXiv: `0907.2997 [hep-ph]` (cit. on p. 4).

[66] R. V. Harlander, H. Mantler, S. Marzani, and K. J. Ozeren, *Higgs production in gluon fusion at next-to-next-to-leading order QCD for finite top mass*, Eur. Phys. J. **C66** (2010) 359, arXiv: `0912.2104 [hep-ph]` (cit. on p. 4).

[67] S. Actis, G. Passarino, C. Sturm, and S. Uccirati, *NLO electroweak corrections to Higgs boson production at hadron colliders*, Phys. Lett. B **670** (2008) 12, arXiv: `0809.1301 [hep-ph]` (cit. on p. 4).

[68] S. Actis, G. Passarino, C. Sturm, and S. Uccirati, *NNLO Computational Techniques: The Cases $H \to \gamma\gamma$ and $H \to gg$*, Nucl. Phys. **B811** (2009) 182, arXiv: `0809.3667 [hep-ph]` (cit. on p. 4).

[69] C. Anastasiou, R. Boughezal, and F. Petriello, *Mixed QCD-electroweak corrections to Higgs boson production in gluon fusion*, JHEP **04** (2009) 003, arXiv: `0811.3458 [hep-ph]` (cit. on p. 4).

[70] U. Aglietti, R. Bonciani, G. Degrassi, and A. Vicini, *Two loop light fermion contribution to Higgs production and decays*, Phys. Lett. B **595** (2004) 432, arXiv: `hep-ph/0404071` (cit. on p. 4).

[71] G. Bozzi, S. Catani, D. de Florian, and M. Grazzini, *Transverse-momentum resummation and the spectrum of the Higgs boson at the LHC*, Nucl. Phys. B **737** (2006) 73, arXiv: `hep-ph/0508068` (cit. on p. 4).

[72] D. de Florian, G. Ferrera, M. Grazzini, and D. Tommasini, *Transverse-momentum resummation: Higgs boson production at the Tevatron and the LHC*, JHEP **11** (2011) 064, arXiv: `1109.2109 [hep-ph]` (cit. on p. 4).

[73] M. Grazzini and H. Sargsyan, *Heavy-quark mass effects in Higgs boson production at the LHC*, JHEP **09** (2013) 129, arXiv: `1306.4581 [hep-ph]` (cit. on p. 4).

[74] P. Nason and C. Oleari, *NLO Higgs boson production via vector-boson fusion matched with shower in POWHEG*, JHEP **02** (2010) 037, arXiv: `0911.5299 [hep-ph]` (cit. on p. 4).

[75] M. Ciccolini, A. Denner, and S. Dittmaier, *Strong and Electroweak Corrections to the Production of a Higgs Boson + 2 Jets via Weak Interactions at the Large Hadron Collider*, Phys. Rev. Lett. **99** (2007) 161803, arXiv: `0707.0381 [hep-ph]` (cit. on p. 4).

[76] M. Ciccolini, A. Denner, and S. Dittmaier, *Electroweak and QCD corrections to Higgs production via vector-boson fusion at the LHC*, Phys. Rev. D **77** (2008) 013002, arXiv: `0710.4749 [hep-ph]` (cit. on p. 4).

[77] P. Bolzoni, F. Maltoni, S.-O. Moch, and M. Zaro, *Higgs Boson Production via Vector-Boson Fusion at Next-to-Next-to-Leading Order in QCD*, Phys. Rev. Lett. **105** (2010) 011801, arXiv: `1003.4451 [hep-ph]` (cit. on p. 4).

[78] G. Cullen et al., *Automated one-loop calculations with GoSam*, Eur. Phys. J. C **72** (2012) 1889, arXiv: `1111.2034 [hep-ph]` (cit. on p. 4).

[79] G. Luisoni, P. Nason, C. Oleari, and F. Tramontano, *HW$^{\pm}$/HZ + 0 and 1 jet at NLO with the POWHEG BOX interfaced to GoSam and their merging within MiNLO*, JHEP **10** (2013) 083, arXiv: `1306.2542 [hep-ph]` (cit. on p. 4).

[80] O. Brein, R. V. Harlander, and T. J. E. Zirke, *vh@nnlo - Higgs Strahlung at hadron colliders*, Comput. Phys. Commun. **184** (2013) 998, arXiv: `1210.5347 [hep-ph]` (cit. on p. 4).

[81] R. V. Harlander, J. Klappert, S. Liebler, and L. Simon, *vh@nnlo-v2: New physics in Higgs Strahlung*, JHEP **05** (2018) 089, arXiv: `1802.04817 [hep-ph]` (cit. on p. 4).

[82] O. Brein, A. Djouadi, and R. Harlander, *NNLO QCD corrections to the Higgs-strahlung processes at hadron colliders*, Phys. Lett. B **579** (2004) 149, arXiv: `hep-ph/0307206` (cit. on p. 4).

[83] O. Brein, R. Harlander, M. Wiesemann, and T. Zirke, *Top-Quark Mediated Effects in Hadronic Higgs-Strahlung*, Eur. Phys. J. C **72** (2012) 1868, arXiv: `1111.0761 [hep-ph]` (cit. on p. 4).

[84] R. V. Harlander, A. Kulesza, V. Theeuwes, and T. Zirke, *Soft gluon resummation for gluon-induced Higgs Strahlung*, JHEP **11** (2014) 082, arXiv: `1410.0217 [hep-ph]` (cit. on p. 4).

[85] G. Ferrera, G. Somogyi, and F. Tramontano, *Associated production of a Higgs boson decaying into bottom quarks at the LHC in full NNLO QCD*, Phys. Lett. **B780** (2018) 346, arXiv: `1705.10304 [hep-ph]` (cit. on p. 4).

[86] F. Caola, G. Luisoni, K. Melnikov, and R. Röntsch, *NNLO QCD corrections to associated WH production and H → b$\bar{b}$ decay*, Phys. Rev. **D97** (2018) 074022, arXiv: `1712.06954 [hep-ph]` (cit. on p. 4).

[87] M. L. Ciccolini, S. Dittmaier, and M. Kramer, *Electroweak radiative corrections to associated WH and ZH production at hadron colliders*, Phys. Rev. **D68** (2003) 073003, arXiv: `hep-ph/0306234 [hep-ph]` (cit. on p. 4).

[88] A. Denner, S. Dittmaier, S. Kallweit, and A. Mück, *Electroweak corrections to Higgs-strahlung off W/Z bosons at the Tevatron and the LHC with HAWK*, JHEP **03** (2012) 075, arXiv: `1112.5142 [hep-ph]` (cit. on p. 4).

[89] A. Denner, S. Dittmaier, S. Kallweit, and A. Mück, *HAWK 2.0: A Monte Carlo program for Higgs production in vector-boson fusion and Higgs strahlung at hadron colliders*, Comput. Phys. Commun. **195** (2015) 161, arXiv: `1412.5390 [hep-ph]` (cit. on p. 4).

[90] L. Altenkamp, S. Dittmaier, R. V. Harlander, H. Rzehak, and T. J. E. Zirke, *Gluon-induced Higgs-strahlung at next-to-leading order QCD*, JHEP **02** (2013) 078, arXiv: `1211.5015 [hep-ph]` (cit. on p. 4).

[91] H. B. Hartanto, B. Jager, L. Reina, and D. Wackeroth, *Higgs boson production in association with top quarks in the POWHEG BOX*, Phys. Rev. D **91** (2015) 094003, arXiv: `1501.04498 [hep-ph]` (cit. on p. 4).

[92] J. Alwall et al., *The automated computation of tree-level and next-to-leading order differential cross sections, and their matching to parton shower simulations*, JHEP **07** (2014) 079, arXiv: `1405.0301 [hep-ph]` (cit. on p. 4).

[93] P. Artoisenet, R. Frederix, O. Mattelaer, and R. Rietkerk, *Automatic spin-entangled decays of heavy resonances in Monte Carlo simulations*, JHEP **03** (2013) 015, arXiv: `1212.3460 [hep-ph]` (cit. on p. 4).

[94] R. D. Ball et al., *Parton distributions for the LHC Run II*, JHEP **04** (2015) 040, arXiv: `1410.8849 [hep-ph]` (cit. on p. 4).

[95] W. Beenakker et al., *NLO QCD corrections to $t\bar{t}H$ production in hadron collisions*, Nucl. Phys. B **653** (2003) 151, arXiv: `hep-ph/0211352` (cit. on p. 4).

[96] S. Dawson, C. Jackson, L. Orr, L. Reina, and D. Wackeroth, *Associated Higgs production with top quarks at the large hadron collider: NLO QCD corrections*, Phys. Rev. D **68** (2003) 034022, arXiv: `hep-ph/0305087` (cit. on p. 4).

[97] Y. Zhang, W.-G. Ma, R.-Y. Zhang, C. Chen, and L. Guo, *QCD NLO and EW NLO corrections to $t\bar{t}H$ production with top quark decays at hadron collider*, Phys. Lett. B **738** (2014) 1, arXiv: `1407.1110 [hep-ph]` (cit. on p. 4).

[98] S. Frixione, V. Hirschi, D. Pagani, H. S. Shao, and M. Zaro, *Weak corrections to Higgs hadroproduction in association with a top-quark pair*, JHEP **09** (2014) 065, arXiv: `1407.0823 [hep-ph]` (cit. on p. 4).

[99] M. Wiesemann et al., *Higgs production in association with bottom quarks*, JHEP **02** (2015) 132, arXiv: `1409.5301 [hep-ph]` (cit. on p. 4).

[100] R. D. Ball et al., *Parton distributions with LHC data*, Nucl. Phys. B **867** (2013) 244, arXiv: `1207.1303 [hep-ph]` (cit. on p. 4).

[101] S. Dawson, C. Jackson, L. Reina, and D. Wackeroth, *Exclusive Higgs boson production with bottom quarks at hadron colliders*, Phys. Rev. D **69** (2004) 074027, arXiv: `hep-ph/0311067` (cit. on p. 4).

[102] S. Dittmaier, M. Krämer, and M. Spira, *Higgs radiation off bottom quarks at the Tevatron and the CERN LHC*, Phys. Rev. D **70** (2004) 074010, arXiv: `hep-ph/0309204` (cit. on p. 4).

[103] R. V. Harlander and W. B. Kilgore, *Higgs boson production in bottom quark fusion at next-to-next-to leading order*, Phys. Rev. D **68** (2003) 013001, arXiv: `hep-ph/0304035` (cit. on p. 4).

[104] J. Pumplin et al., *New generation of parton distributions with uncertainties from global QCD analysis*, JHEP **07** (2002) 012, arXiv: `hep-ph/0201195` (cit. on p. 4).

[105] F. Demartin, F. Maltoni, K. Mawatari, and M. Zaro, *Higgs production in association with a single top quark at the LHC*, Eur. Phys. J. C **75** (2015) 267, arXiv: `1504.00611 [hep-ph]` (cit. on p. 4).

[106] F. Demartin, B. Maier, F. Maltoni, K. Mawatari, and M. Zaro, *tWH associated production at the LHC*, Eur. Phys. J. **C77** (2017) 34, arXiv: `1607.05862 [hep-ph]` (cit. on p. 4).

[107] T. Sjöstrand, S. Mrenna, and P. Z. Skands, *A brief introduction to PYTHIA 8.1*, Comput. Phys. Commun. **178** (2008) 852, arXiv: `0710.3820 [hep-ph]` (cit. on p. 4).

[108] S. Gieseke, A. Ribon, M. H. Seymour, P. Stephens, and B. Webber, *Herwig++ 1.0: an event generator for e+e- annihilation*, JHEP **02** (2004) 005, arXiv: `hep-ph/0311208` (cit. on p. 4).

[109] ATLAS Collaboration, *Measurement of the Z/γ^* boson transverse momentum distribution in pp collisions at $\sqrt{s}$ = 7 TeV with the ATLAS detector*, JHEP **09** (2014) 145, arXiv: `1406.3660 [hep-ex]` (cit. on p. 4).

[110] ATLAS Collaboration, *ATLAS Pythia 8 tunes to 7 TeV data*, ATL-PHYS-PUB-2014-021, 2014, URL: `https://cds.cern.ch/record/1966419` (cit. on p. 4).

[111] A. Djouadi, J. Kalinowski, and M. Spira, *HDECAY: A Program for Higgs boson decays in the Standard Model and its supersymmetric extension*, Comput. Phys. Commun. **108** (1998) 56, arXiv: `hep-ph/9704448` (cit. on p. 5).

[112] M. Spira, *QCD effects in Higgs physics*, Fortsch. Phys. **46** (1998) 203, arXiv: `hep-ph/9705337 [hep-ph]` (cit. on p. 5).

[113] A. Djouadi, M. M. Mühlleitner, and M. Spira, *Decays of supersymmetric particles: The Program SUSY-HIT (SUspect-SdecaY-Hdecay-InTerface)*, Acta Phys. Polon. B **38** (2007) 635, arXiv: `hep-ph/0609292` (cit. on p. 5).

[114] A. Bredenstein, A. Denner, S. Dittmaier, and M. Weber, *Radiative corrections to the semileptonic and hadronic Higgs-boson decays $H \rightarrow WW/ZZ \rightarrow 4$ fermions*, JHEP **02** (2007) 080, arXiv: `hep-ph/0611234` (cit. on p. 5).

[115] A. Bredenstein, A. Denner, S. Dittmaier, and M. Weber, *Precise predictions for the Higgs-boson decay $H \rightarrow WW/ZZ \rightarrow 4$ leptons*, Phys. Rev. D **74** (2006) 013004, arXiv: `hep-ph/0604011` (cit. on p. 5).

[116] A. Bredenstein, A. Denner, S. Dittmaier, and M. M. Weber, *Precision calculations for the Higgs decays H —> ZZ/WW —> 4 leptons*, Nucl. Phys. Proc. Suppl. **160** (2006) 131, [,131(2006)], arXiv: `hep-ph/0607060 [hep-ph]` (cit. on p. 5).

[117] H.-L. Lai et al., *New parton distributions for collider physics*, Phys. Rev. D **82** (2010) 074024, arXiv: `1007.2241 [hep-ph]` (cit. on p. 5).

[118] E. Bagnaschi, G. Degrassi, P. Slavich, and A. Vicini, *Higgs production via gluon fusion in the POWHEG approach in the SM and in the MSSM*, JHEP **02** (2012) 088, arXiv: `1111.2854 [hep-ph]` (cit. on p. 5).

[119] S. Agostinelli et al., *GEANT4—a simulation toolkit*, Nucl. Instrum. Methods **506** (2003) 250 (cit. on p. 5).

[120] ATLAS Collaboration, *The ATLAS Simulation Infrastructure*, Eur. Phys. J. C **70** (2010) 823, arXiv: 1005.4568 [physics.ins-det] (cit. on p. 5).

[121] A. Martin, W. Stirling, R. Thorne, and G. Watt, *Parton distributions for the LHC*, Eur. Phys. J. C **63** (2009) 189, arXiv: 0901.0002 [hep-ph] (cit. on p. 5).

[122] ATLAS Collaboration, *Summary of ATLAS Pythia 8 tunes*, ATL-PHYS-PUB-2012-003, 2012, URL: https://cds.cern.ch/record/1474107 (cit. on p. 5).

[123] ATLAS Collaboration, *The Pythia 8 A3 tune description of ATLAS minimum bias and inelastic measurements incorporating the Donnachie–Landshoff diffractive model*, ATL-PHYS-PUB-2016-017, 2016, URL: https://cds.cern.ch/record/2206965 (cit. on p. 5).

[124] ATLAS Collaboration, *Observation of $H \to b\bar{b}$ decays and VH production with the ATLAS detector*, Phys. Lett. B **786** (2018) 59, arXiv: 1808.08238 [hep-ex] (cit. on p. 7).

[125] ATLAS Collaboration, *Measurement of VH, $H \to b\bar{b}$ production as a function of the vector-boson transverse momentum in* 13 *TeV pp collisions with the ATLAS detector*, JHEP **05** (2019) 141, arXiv: 1903.04618 [hep-ex] (cit. on p. 7).

[126] R. J. Barlow and C. Beeston, *Fitting using finite Monte Carlo samples*, Comput. Phys. Commun. **77** (1993) 219 (cit. on p. 8).

[127] K. Cranmer, G. Lewis, L. Moneta, A. Shibata, and W. Verkerke, *HistFactory: A tool for creating statistical models for use with RooFit and RooStats*, CERN-OPEN-2012-016 (2012), URL: http://cdsweb.cern.ch/record/1456844 (cit. on p. 8).

[128] G. Cowan, K. Cranmer, E. Gross, and O. Vitells, *Asymptotic formulae for likelihood-based tests of new physics*, Eur. Phys. J. C **71** (2011) 1554, arXiv: 1007.1727 [physics.data-an], Erratum: Eur. Phys. J. C73 (2013) 2501 (cit. on pp. 9, 10).

[129] A. L. Read, *Presentation of search results: the CL_s technique*, J. Phys. G **28** (2002) 2693 (cit. on p. 9).

[130] ATLAS Collaboration, *Evaluation of theoretical uncertainties for simplified template cross section measurements of V-associated production of the Higgs boson*, ATL-PHYS-PUB-2018-035, 2018, URL: https://cds.cern.ch/record/2649241 (cit. on p. 21).

[131] ALEPH, CDF, D0, DELPHI, L3, OPAL, SLD Collaborations; LEP and Tevatron Electroweak Working Group; and SLD Electroweak and Heavy Flavour Groups, *Precision Electroweak Measurements and Constraints on the Standard Model*, (2010), arXiv: 1012.2367 [hep-ex] (cit. on p. 39).

[132] T. D. Lee, *A Theory of Spontaneous T Violation*, Phys. Rev. D **8** (1973) 1226 (cit. on p. 40).

[133] J. F. Gunion and H. E. Haber, *The CP conserving two Higgs doublet model: The Approach to the decoupling limit*, Phys. Rev. D **67** (2003) 075019, arXiv: hep-ph/0207010 (cit. on p. 40).

[134] G. Branco et al., *Theory and phenomenology of two-Higgs-doublet models*, Phys. Rept. **516** (2012) 1, arXiv: 1106.0034 [hep-ph] (cit. on pp. 40, 41).

[135] S. L. Glashow and S. Weinberg, *Natural Conservation Laws for Neutral Currents*, Phys. Rev. D **15** (1977) 1958 (cit. on p. 40).

[136] E. A. Paschos, *Diagonal Neutral Currents*, Phys. Rev. D **15** (1977) 1966 (cit. on p. 40).
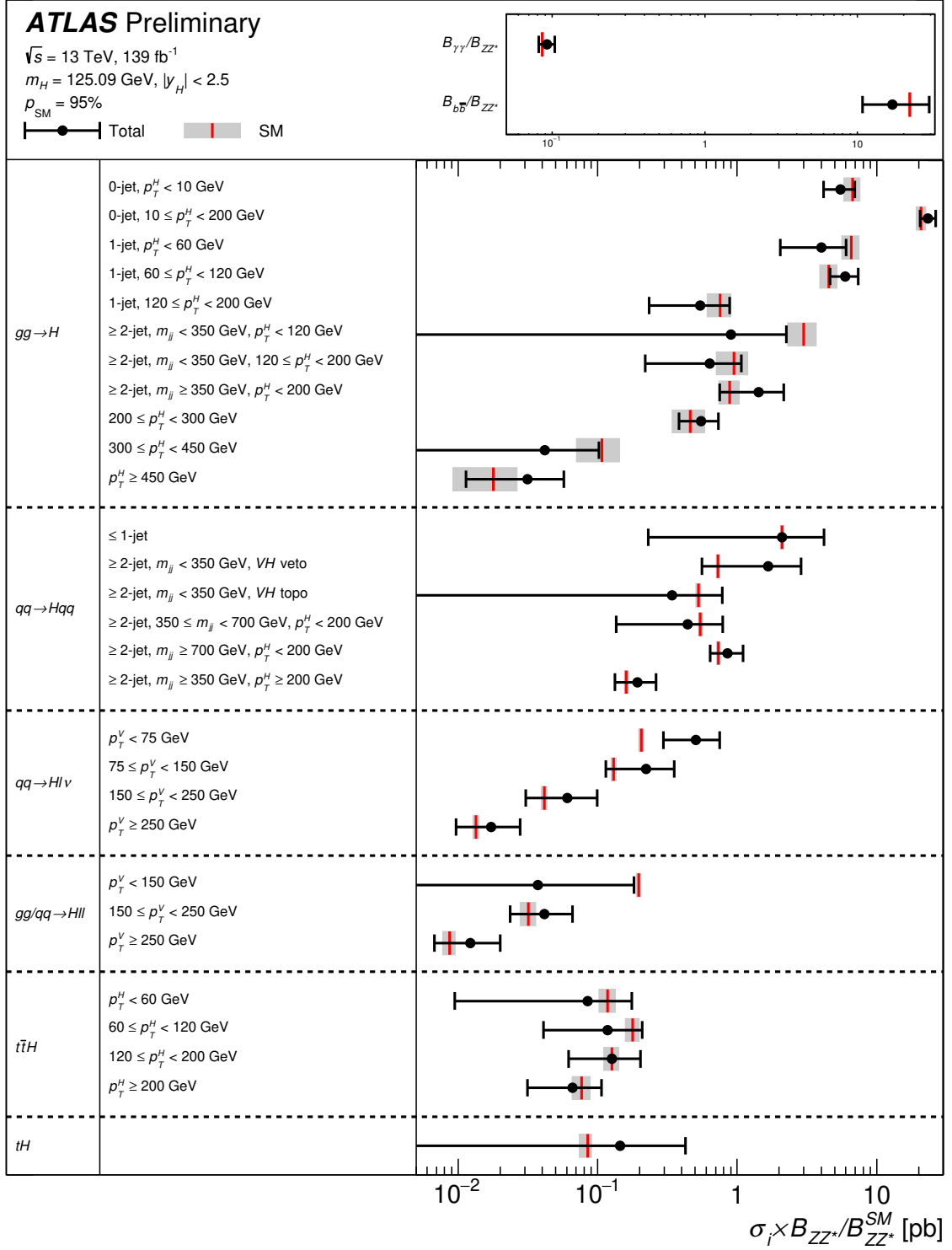
Appendix

Figure 18: Best-fit values and uncertainties for the cross sections in each measurement region and of the ratios of branching fractions B_f/B_{ZZ}. The parameters directly extracted from the fit are the products ($\sigma_i \times B_{ZZ}$) and the ratios B_f/B_{ZZ}; the former are shown divided by the SM value of B_{ZZ}. The black error bar shows the total uncertainty in each measurement. The level of compatibility between the combined measurement and the SM prediction, estimated using the procedure outlined in the text with 31 degrees of freedom, corresponds to a p-value of $p_{SM} = 95\%$.
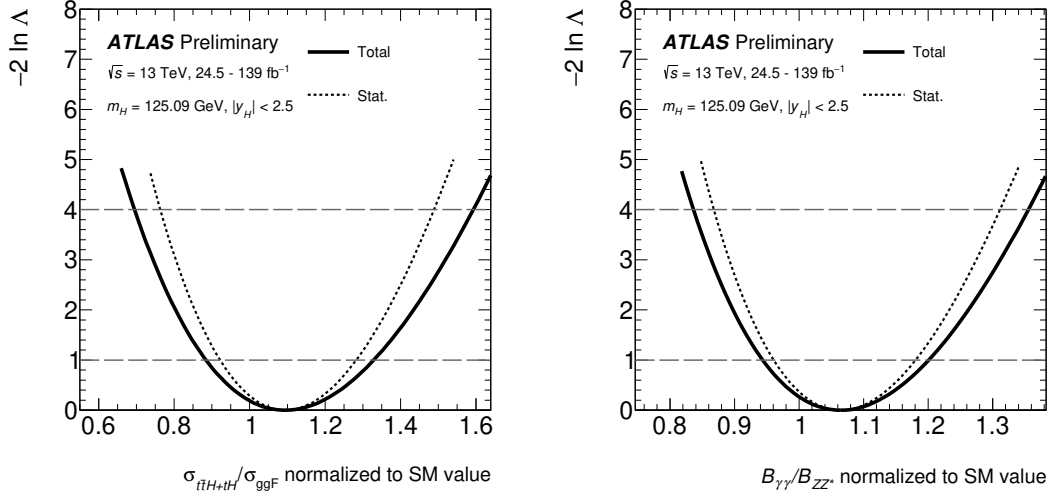
Figure 19: The observed negative log-likelihood scans as a function of (a) $\sigma_{t\bar{t}H+tH}/\sigma_{ggF}$ and (b) $B_{\gamma\gamma}/B_{ZZ}$ measured using a generic parameterization in terms of ratios of cross sections and branching fractions. All the other parameters of interest from the model are also varied in the minimization procedure. Variations of the test statistic with all systematic uncertainties included (solid line), and with parameters describing systematic uncertainties fixed to their best-fit values (dotted line). The dashed horizontal lines show the levels $-2\ln\Lambda = 1$ and $-2\ln\Lambda = 4$ which are used to define, respectively, the 1σ and 2σ confidence intervals for the parameter of interest.
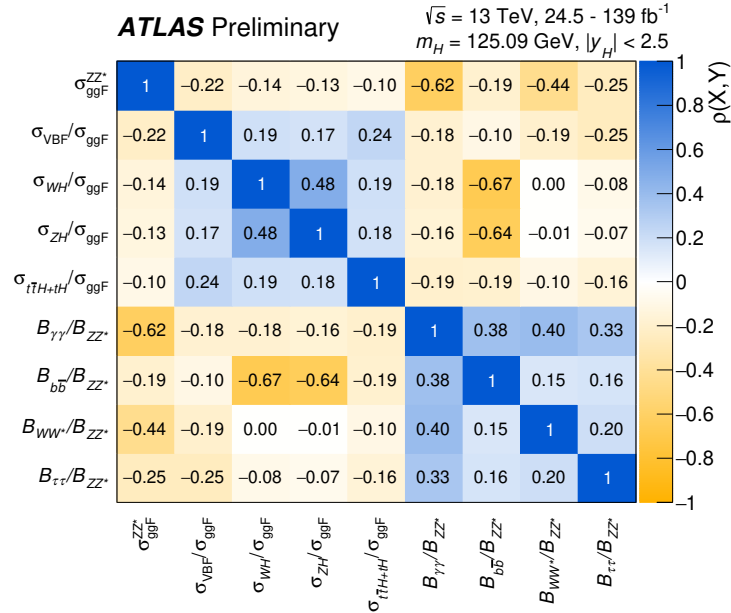
Figure 20: Correlation matrix for the measured values of σ_{ggF}^{ZZ}, $\sigma_{VBF}/\sigma_{ggF}$, σ_{WH}/σ_{ggF}, σ_{ZH}/σ_{ggF}, $\sigma_{t\bar{t}H+tH}/\sigma_{ggF}$, $B_{\gamma\gamma}/B_{ZZ}$, B_{WW}/B_{ZZ}, $B_{\tau\tau}/B_{ZZ}$, and B_{bb}/B_{ZZ}.
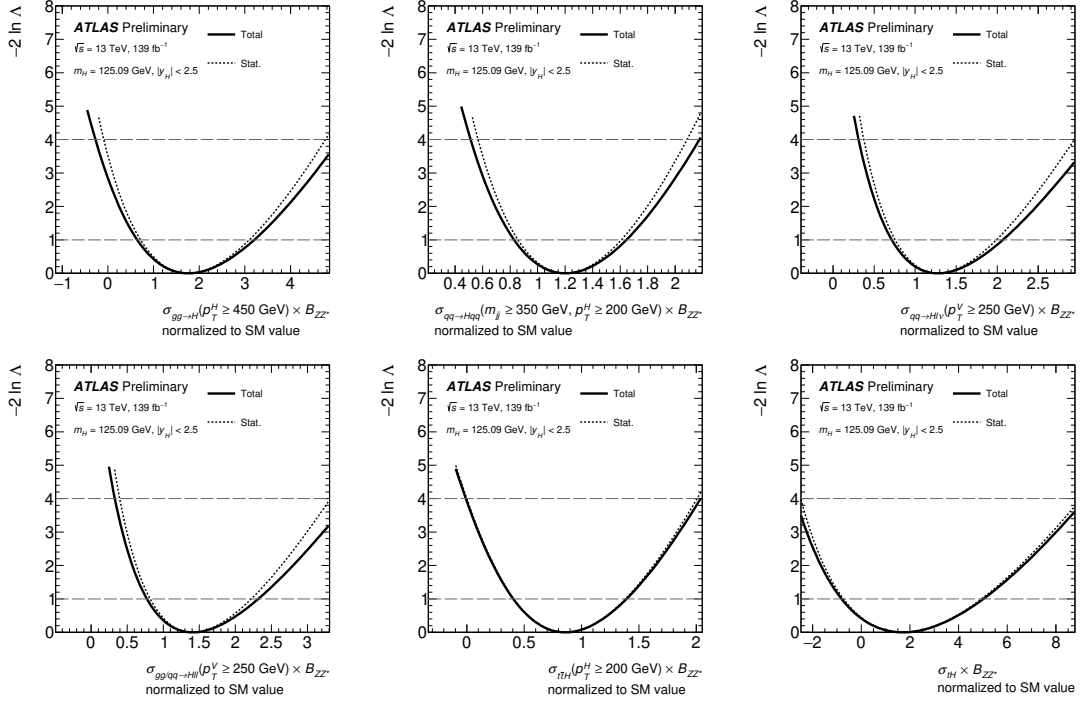
Figure 21: The observed negative log-likelihood scans as a function of (a) $\sigma_{gg \to H}(p_T^H \geq 450\,\text{GeV}) \times B_{ZZ}$, (b) $\sigma_{qq \to Hqq}(m_{jj} \geq 350\,GeV,\ p_T^H \geq 200\,\text{GeV}) \times B_{ZZ}$, (c) $\sigma_{qq \to H\ell\nu}(p_T^V \geq 250\,\text{GeV}) \times B_{ZZ}$, (d) $\sigma_{gg/qq \to H\ell\ell}(p_T^V \geq 250\,\text{GeV}) \times B_{ZZ}$, (e) $\sigma_{t\bar{t}H}(p_T^H \geq 200\,\text{GeV}) \times B_{ZZ}$, and (f) $\sigma_{tH} \times B_{ZZ}$, with all normalized to SM predictions measured in the STXS framework. All the other parameters of interest from the model are also varied in the minimization procedure. Variations of the test statistic with all systematic uncertainties included (solid line), and with parameters describing systematic uncertainties fixed to their best-fit values (dotted line). The dashed horizontal lines show the levels $-2\ln\Lambda = 1$ and $-2\ln\Lambda = 4$ which are used to define, respectively, the $1\,\sigma$ and $2\,\sigma$ confidence intervals for the parameter of interest.
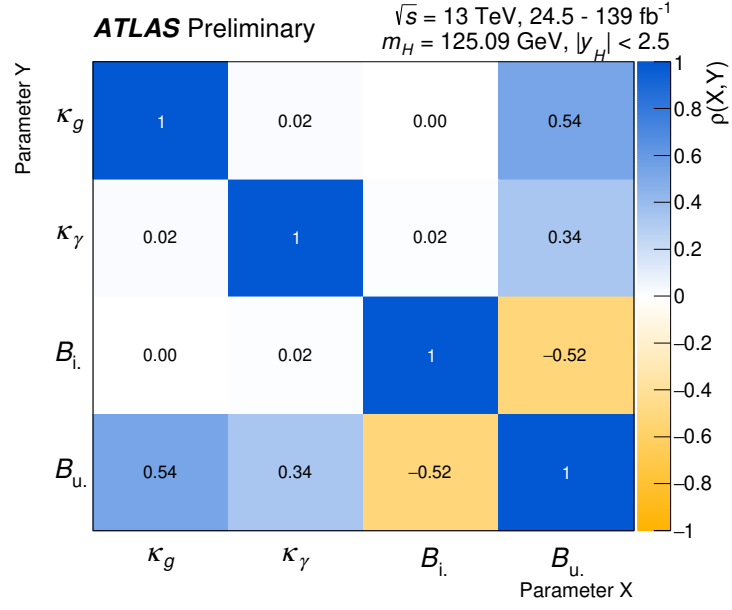
Figure 22: Correlation matrix for the measured values of κ_g, κ_γ, $B_{\mathrm{i.}}$, and $B_{\mathrm{u.}}$.

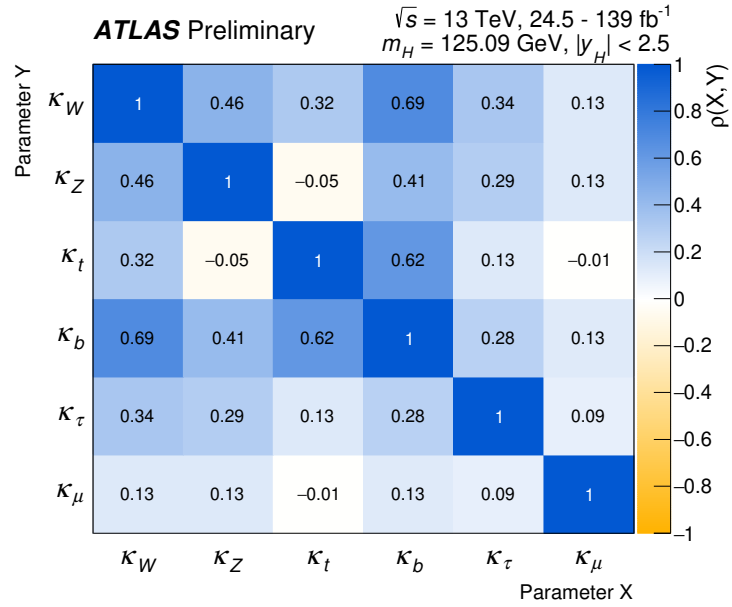Figure 23: Correlation matrix for the measured values of κ_t, κ_Z, κ_W, κ_b, κ_τ, and κ_μ.
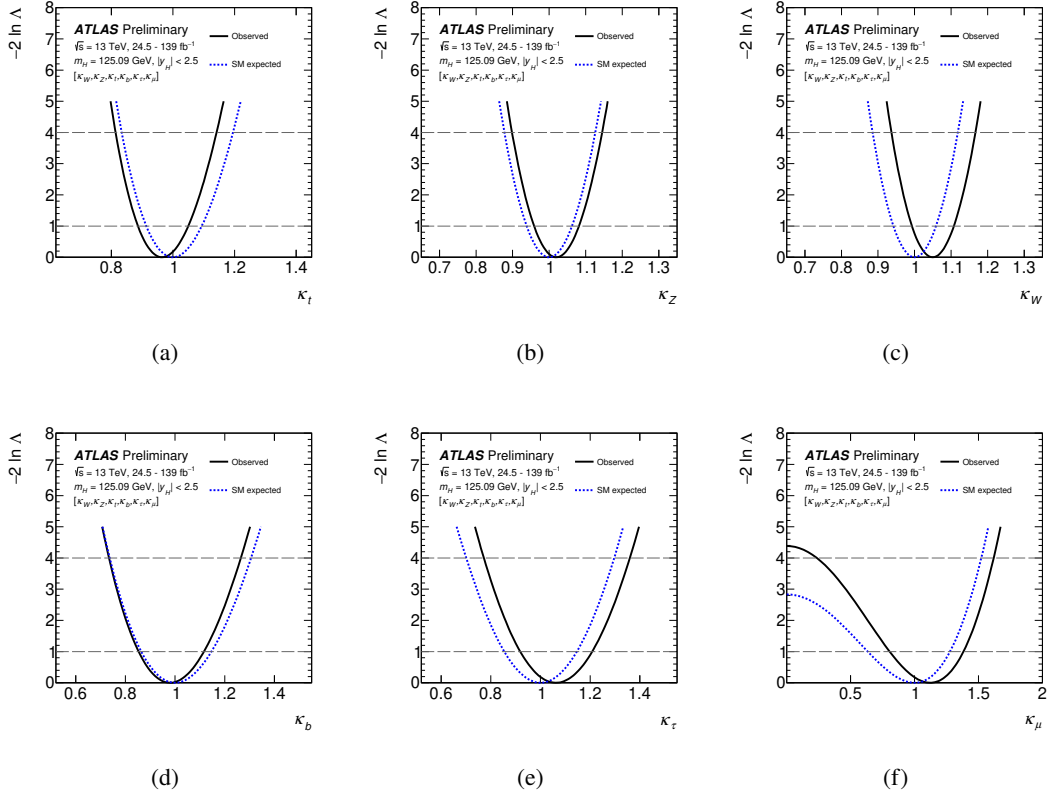
Figure 24: Observed (solid line) and expected (dotted line) negative log-likelihood scans as a function of (a) κ_t, (b) κ_Z, (c) κ_W, (d) κ_b, (e) κ_τ, and (f) κ_μ from a combined fit of these six parameters. When scanning one parameter, other parameters of interest from the model are also varied in the minimization procedure. The dashed horizontal lines show the levels $-2 \ln \Lambda = 1$ and $-2 \ln \Lambda = 4$ which are used to define, respectively, the $1\,\sigma$ and $2\,\sigma$ confidence intervals for the parameter of interest.

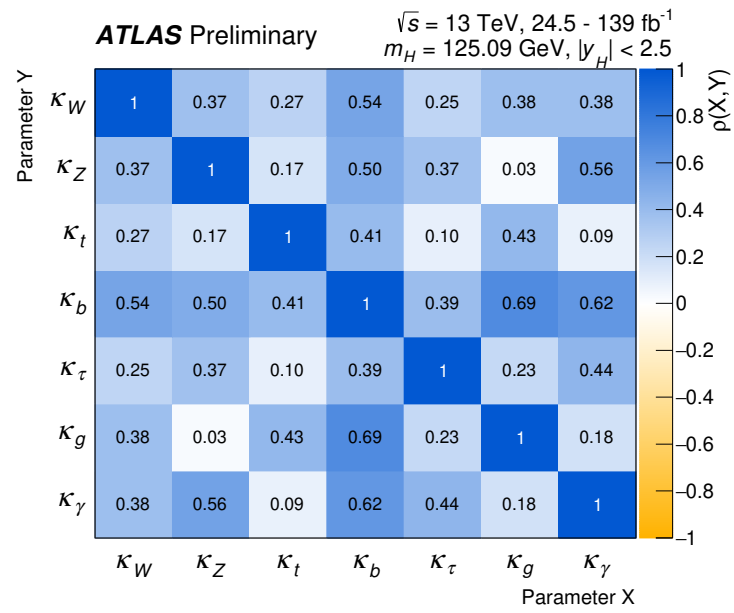Figure 25: Correlation matrix for the measured values of κ_Z, κ_W, κ_t, κ_b, κ_τ, κ_g, and κ_γ.
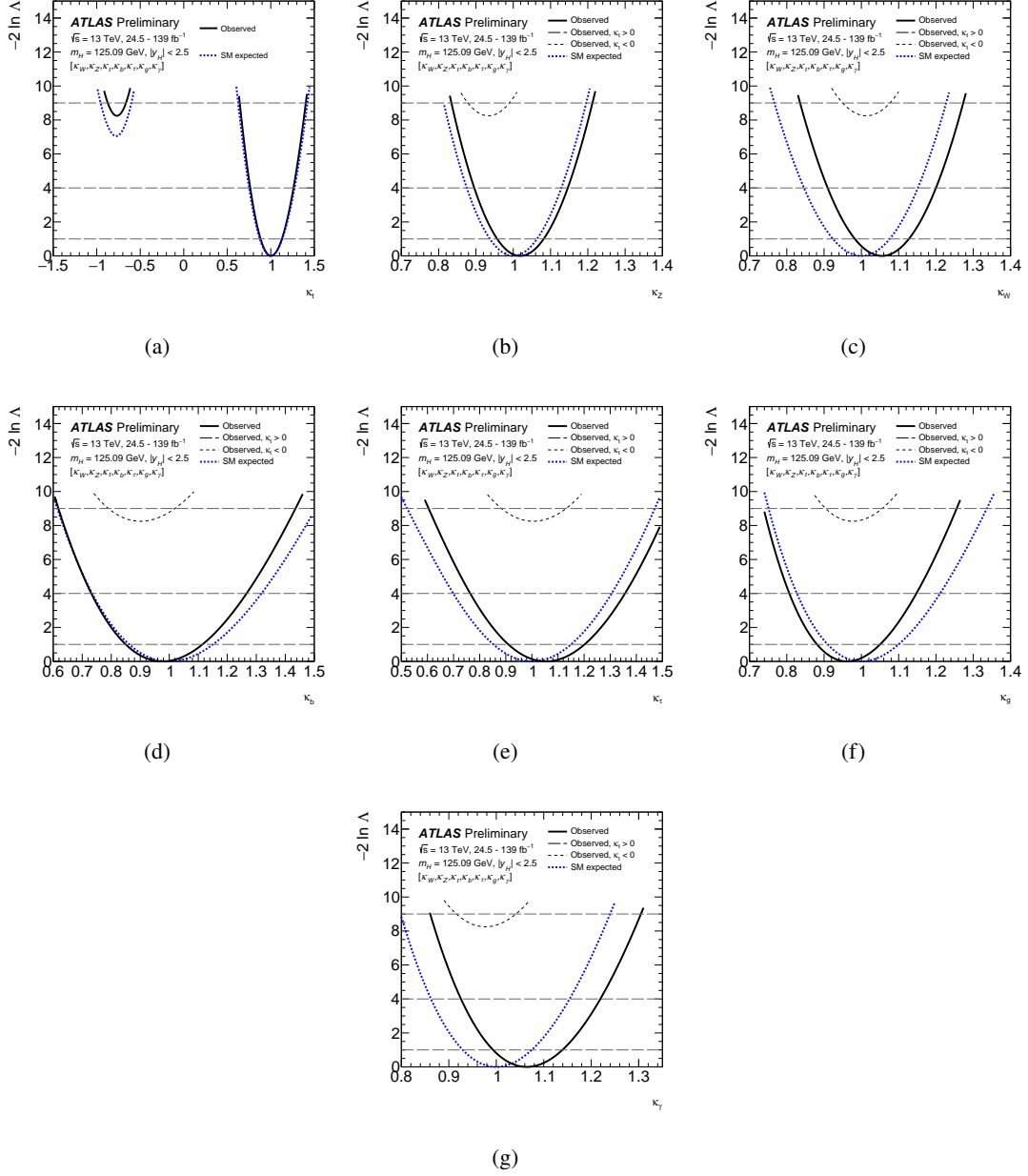
(a)

(b)

(c)

(d)

(e)

(f)

(g)

Figure 26: Observed (solid line) and expected (dotted line) negative log-likelihood scans as a function of (a) κ_t, (b) κ_Z, (c) κ_W, (d) κ_b, (e) κ_τ, (f) κ_g, and (g) κ_γ from a combined fit of these seven parameters. When scanning one parameter, other parameters of interest from the model are also varied in the minimization procedure. The dashed horizontal lines show the levels $-2\ln\Lambda = 1$, $-2\ln\Lambda = 4$, and $-2\ln\Lambda = 9$ which are used to define, respectively, the $1\,\sigma$, $2\,\sigma$, and $3\,\sigma$ confidence intervals for the parameter of interest.
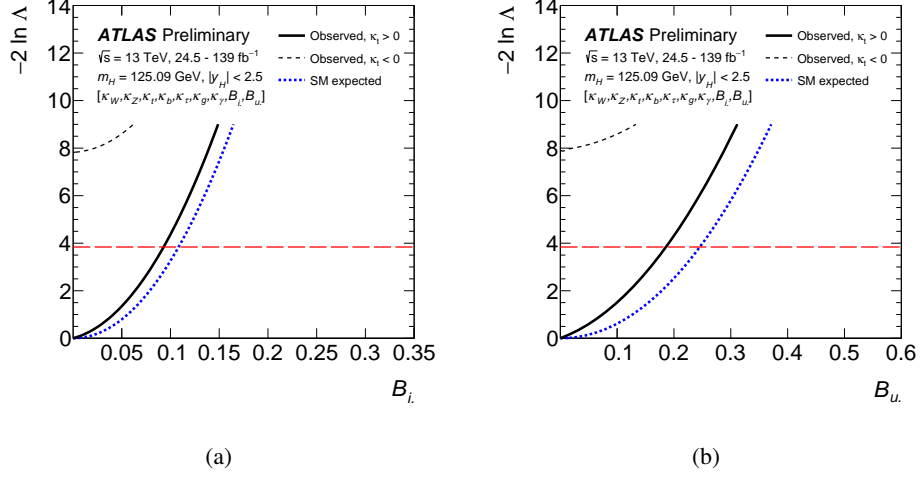
Figure 27: Observed (solid line) and expected (dotted line) negative log-likelihood scans as a function of (a) $B_{\mathrm{i.}}$ and (b) $B_{\mathrm{u.}}$ from a combined fit including the search for Higgs boson decays into invisible final states with a generic parameterization involving coupling strengths to SM particles as well as loop-induced ggH and $H \to \gamma\gamma$ vertices. All the other parameters of interest from the model are also varied in the minimization procedure. The dashed horizontal line shows the level used to obtain the 95% CL limit.
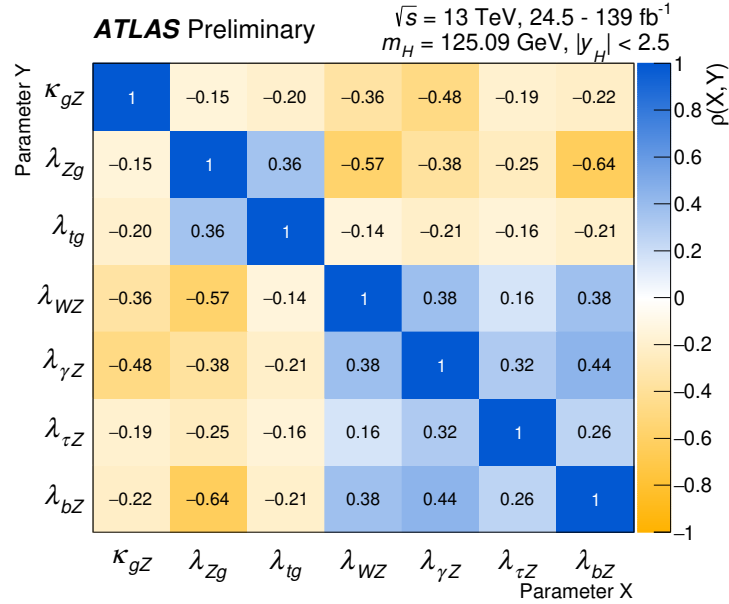

Figure 28: Correlation matrix for the measured values of κ_{gZ}, λ_{Zg}, λ_{tg}, λ_{WZ}, $\lambda_{\gamma Z}$, $\lambda_{\tau Z}$, and λ_{bZ}.